CHALMERS
UNIVERSITY OF TECHNOLOGY

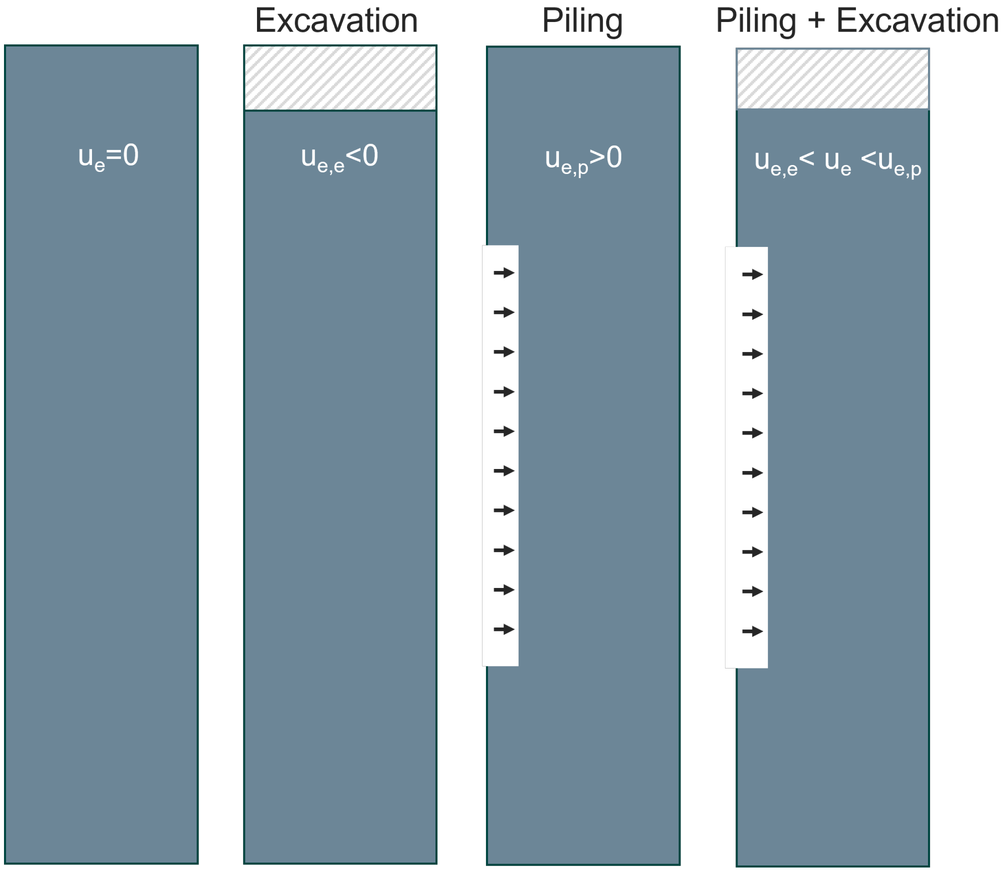

Analysis of excess pore pressure evolution during and following excavation and piling in soft clay

Master's thesis in Master Program Infrastructure and Environmental Engineering

Viktor Lundqvist
Annie Sylvén Stålhandske

Department of Architecture and Civil Engineering
CHALMERS UNIVERSITY OF TECHNOLOGY
Master's thesis ACEX30
Gothenburg, Sweden 2024

Master's thesis ACEX30

Analysis of excess pore pressure evolution during and following excavation and piling in soft clay

Viktor Lundqvist
Annie Sylvén Stålhandske

CHALMERS
UNIVERSITY OF TECHNOLOGY

Department of Architecture and Civil Engineering
Division of Geology and Geotechnics
Chalmers University of Technology
Gothenburg, Sweden 20124

Analysis of excess pore pressure evolution during and following excavation and piling in soft clay

Viktor Lundqvist
Annie Sylvén Stålhandske

Supervisor: Johannes Tornborg, Department of Architecture and Civil Engineering, Division of Geology and Geotechnics, Chalmers and Skanska.
Supervisor: David Nguyen, Skanska.
Supervisor: Anders Kullingsjö, Skanska.
Examiner: Mats Karlsson, Department of Architecture and Civil Engineering, Division of Geology and Geotechnics, Chalmers.

Department of Architecture and Civil Engineering
Division Geology and Geotechnics
Chalmers University of Technology
SE-412 96 Gothenburg
Telephone +46 31 772 1000

Cover: Conceptual image illustrating the hypotheses of this study, the evolution of excess pore pressure generated during pile installation, and excavation processes, separately and combined.

Department of Architecture and Civil Engineering
Gothenburg, Sweden 2024

Analysis of excess pore pressure evolution during and following excavation and piling in soft clay
Viktor Lundqvist
Annie Sylvén Stålhandske
Department of Architecture and Civil Engineering
Division of Geology and Geotechnics
Chalmers University of Technology

Abstract

This thesis aims to study the combined impact of pile driving and excavation have on the development and evolution of excess pore pressure, heave, and heave pressure. To fulfill this aim, numerical analyses were conducted to simulate the pore pressure evolution and heave during pile driving and excavation processes. Two constitutive models were used, a Mohr-Coulomb model and the Modified Cam Clay model. Two numerical models were first constructed simulating excavating and piling respectively, where a cavity expansion was used to simulate the pile installation. The results from these models were validated against analytical solutions found in the literature to verify that the pile driving and unloading, yielded results that were consistent with theory. After these models had been validated, a new model simulating both excavating and piling was constructed. The computed results from this model were compared to monitored pore pressure data from an existing construction site, located in Gothenburg, Sweden. Thereafter, a parametric study was conducted to generalise the result by varying the permeability and stiffness. The results indicate that piling before excavating reduces the heave pressure, compared to only excavating. Furthermore, results also indicate that piling before excavating, generates less vertical displacements at the excavation bottom, compared to to the reverse construction sequence (i.e piling after excavating). As the piling model in this thesis only simulated the cavity expansion and not the pile material, the reinforcing effect piles have on heave would be of interest to study in future research. Further research could also analyse the effect of a group of piles, with regard to pore pressure, heave and heave pressure.

Keywords: Heave pressure, Unloading, Excavation, Piling, Pore pressure, Cavity expansion, Numerical modeling, Mohr-Coulomb, Modified Cam Clay

Analys av portrycksutveckling till följd av pålning och schaktning i lös lera.
Viktor Lundqvist
Annie Sylvén Stålhandske
Institutionen för Arkitektur och Samhällsbyggnadsteknik
Avdelningen för Geologi och Geoteknik
Chalmers University of Technology

Sammanfattning

Detta examensarbete syftar till att studera den kombinerade påverkan som pålning och schaktning har på utvecklingen av portryck, hävning och hävningstryck. För att uppfylla detta syfte utfördes numeriska analyser för att simulera portrycksutveckling och hävning under pålnings- och schaktningsprocesser. Två materialmodeller användes, Modified Cam Clay och Mohr-Coulomb. Två separata numeriska modeller skapades först för att simulera respektive schaktning och pålning, där en "Cavity Expansion" användes för att simulera pålningen. Resultaten från dessa modeller validerades mot analytiska metoder från literatur studien, för att verifiera att pålnings- och schaktningssmodellen ger resultat som överensstämmer med teorin. Efter att dessa modeller hade validerats, skapades en ny modell som simulerade både schaktning och pålning. Beräkningsresultaten från denna modell jämfördes med fältmätningar av portryck från en byggarbetsplats, belägen i Göteborg. Därefter genomfördes en parametrisk studie för att generalisera resultatet genom att variera permeabiliteten och styvheten. Resultaten indikerar att pålning före schaktning minskar portrycket jämfört med enbart schaktning. Dessutom visar resultaten att pålning före schaktning genererar mindre vertikala deformationer i schaktbotten jämfört med den omvända byggordningen (dvs. pålning efter schaktning). Eftersom pålningsmodellen i denna avhandling endast simulerade en cavity expansion, och därmed inget pålelement, skulle det i framtida studier på detta område vara av intresse att simulera ett pålelement. Detta skulle kunna simulera den armerade effekt som kan observeras efter pålinstallation, med avseende på hävning och hävningstryck. Ytterligare studier kan även undersöka pålgruppers effekt på porövertryck, hävning och hävningstryck.

Acknowledgements

This Masters Thesis was conducted at the Department of Architecture and Civil Engineering, at Chalmers University of Technology and in collaboration with Skanska Teknik.

We would like to sincerely thank our supervisors at Skanska David Nguyen and Anders Kullingsjö, and the examiner at Chalmers, Mats Karlsson, for their support and guidance throughout the process of writing this thesis. A special thanks to our supervisor from Chalmers Johannes Tornborg (Industrial PhD student from Skanska), who has been of great support, amidst the completion of his own dissertation. We would also like to express our sincere appreciation to everyone at the geotechnics department at Skanska Teknik, for their support and interest in our work, and for making us feel welcome from day one.

Viktor Lundqvist & Annie Sylvén Stålhandske, June 2024.

Contents

List of Figures **xv**

List of Tables **xvii**

1 Introduction **1**
1.1 Background 1
1.2 Aim and Objectives 2
1.3 Limitations 3

2 Theory **5**
2.1 Pore pressure change in low permeable soils 5
2.2 Compressibility and consolidation 6
2.3 Unloading and heave 7
2.4 Heave pressure in soft clays 9
2.5 Excess pore pressure due to pile driving 10
2.6 Dissipation of excess pore pressures 12
2.7 Numerical modelling 15

3 Case study **27**
3.1 Soil Characteristics 27
3.2 Pore pressure sensors 28
3.3 Construction process 29

4 Method **33**
4.1 Pore pressure data, Brf. Sydney 33
4.2 Analytical calculations 34
4.3 Numerical modeling 37

5 Result **47**
5.1 Pore pressure data, Brf. Sydney. 47
5.2 Piling response 51
5.3 Excavation and pile installation in combination, with a construction time corresponding to Brf. Sydney 56

6 Discussion **67**
6.1 Measured pore pressure data 67
6.2 Piling 68

6.3 Unloading 69
6.4 Constitutive models 70

7 Conclusions and recommendations 73

Bibliography 75

Nomenclature

Abbreviations

AMSL	Above Mean Sea Level
CSL	Critical State Line
EHP	Effective Heave Pressure
M-C	Mohr Coulomb
MCC	Modified Cam Clay
OCR	Over Consolidation Ratio

Greek letters

γ	unit weight
κ	swelling index
λ	compression index
ν	Poisson's ratio
ψ	dilatancy angle
σ	total stress
σ'	effective stress
σ'_h	effective horizontal stress
$\sigma'_{n.center}$	effective vertical stress at center of slab
σ'_v	effective vertical stress
σ_c	pre-consolidation stress
σ_f	normal stress on the failure plane
σ_1	major principal stress
σ_3	minor principal stress
σ_h	horizontal stress
σ_v	vertical stress
τ_f	shear strength
φ	internal friction angle

Roman letters

a_s	swelling index

c'	effective cohesion
c_u	undrained shear strength
E	Young's modulus
G	shear modulus
H	excavation depth
k	hydraulic conductivity (but in this report referred to as permeability)
K_0	earth pressure coefficient at rest
M	oedometer modulus
M_0	compression modulus if $\sigma'_c > (\Delta\sigma + \sigma'_0)$
M_L	compression modulus if $\sigma'_c < (\Delta\sigma + \sigma'_0)$
M_{ul}	unloading Modulus
p'	mean effective stress
q	deviatoric stress
r	radius of the cavity
r_{pl}	radial distance of the plastic zone from the centre of the cavity
$t_{exc.toslab}$	time between finalised excavation and casting the slab
u	pore water pressure
u_e	excess pore water pressure
u_s	steady state, static pore water pressure
y_{min}	depth to bottom of soil layer

List of Figures

2.1 Illustration of the plastic zone around a pile represented by a cavity. Inspired by Hintze et al. (1997) 10
2.2 Variation of excess pore pressure at the pile face with time, from Randolph and Wroth (1979) (Permission for reuse granted by John Wiley & Sons (Wiley)). 12
2.3 Variation of radial distribution of excess pore pressure with time after pile driving in soil with $G/c_u = 50$, from Randolph and Wroth (1979) (Permission for reuse granted by John Wiley & Sons (Wiley)). 13
2.4 Variation of radial distribution of excess pore pressure with time after pile driving in soil with $G/c_u = 100$, from Randolph (2003).(Permission for reuse granted by Emerald Publishing Limited. 14
2.5 Examples of a plane strain (left) and axisymmetrical problem (right) (Inspired by Bentley (2023a)). 15
2.6 Mohr's circle, inspired by Verruijt (2017) 17
2.7 Mohr-Coulomb in principal stress space (retrieved from Sun et al. (2006)) (Permission for reuse granted by Elsevier). 17
2.8 Yield locus of MCC model along with the Critical state line, based on Muir Wood (2004) 20
2.9 Compression and unloading-reloading lines, linear void ratio versus log mean effective stress, based on Muir Wood (2004) 22

3.1 Overview of Masthuggskajen, Brf. Sydney is located at number 18 (retrieved from Masthuggskajen, 2024-01-24). 27
3.2 Position of the piezometers within the construction site (modified technical drawing, G-15-1-0001 (Skanska Teknik, 2023). 29
3.3 Partition of zones during second excavation phase (from +0.6 m to -1.8 m), with dates of respective excavation span (modified technical drawing, G-15-1-0001 (Skanska Teknik, 2023)). 30
3.4 Pile installation reported per week at Brf. Sydney, the figure was generated with knowledge from propile about installation dates and the technical drawing, K-15-1-0080 31

4.1 Location of the simulated unit cell. (Modified technical drawing, K-15-1-0001 (Skanska Teknik, 2023). 39
4.2 Geometry of numerical model corresponding to unit cell in Figure 4.1 (not to scale). 39
4.3 Comparison of calculated CRS-tests and measured 42

4.4 Increase of stiffness versus depth 43

5.1 Excess pore pressure development during excavation, field monitoring data. See Figure 3.3 for the location of excavation areas within the site. 48
5.2 Analytical calculations of excess pore pressure results, compared to monitoring data. (A) denotes analytically calculated excess pore pressures (see section 4.2). 49
5.3 Excess pore pressure development during pile installation, data from Brf. Sydney. 50
5.4 Installation dates of piles in close proximity to the piezometers. . . . 50
5.5 Calculated initial radial variation of excess pore pressures. 52
5.6 Variation of excess pore pressures at pile face with time, for different depths. 53
5.7 Variation of excess pore pressures with time, using Mohr-Coulomb material model 55
5.8 Variation of excess pore pressures with time, using Modified Cam clay material model. 55
5.9 Normalised effective heave pressure at center of slab, versus normalised time (inspired by Tornborg et al., 2024) 57
5.10 Variation of computed excess pore pressures at 3 meters from the pile, construction order corresponding to Brf. Sydney, see table 4.7, i.e. excavation before piling. a) Linear time axis. b) Logarithmic time axis. 59
5.11 Variation of computed excess pore pressures at 3 meters from the pile, with the reverse construction order, i.e. piling before excavation. a) Linear time axis. b) Logarithmic time axis. 61
5.12 Excess pore pressures throughout the model, during stages 1 to 4, for the reversed construction order (See Table 4.7). In Plaxis the sign convention is reversed, thus negative values correspond to positive excess pore pressures. 62
5.13 Vertical displacement below the excavation bottom for the Brf. Sydney case, see Table 4.7. 63
5.14 Vertical displacement below the excavation bottom for the reversed case, see Table 4.7. 63
5.15 Pore pressure over time, measured at Brf. Sydney and computed from the numerical model 64
5.16 Impact of permeability on EHP (P+U denoted piling before excavation) 65
5.17 Impact of stiffness on EHP (P+U denotes piling+excavation) 66

List of Tables

2.1 Stiffness and strength parameters used by the M-C model in Plaxis 2D (Bentley, 2023a) 17
2.2 Parameters of the MCC model in Plaxis 2D (Bentley, 2023a) 22

3.1 Dimensions, unit weights, and strength parameters of the different soil layers, retrieved from Skanska (2022b) 28

4.1 Undrained shear strengths c_u at each respective depth used in the analytical calculations. Values retrieved from Skanska (2022a). 36
4.2 Boundary conditions of the unit cell, used in the numerical model. . . 39
4.3 General input parameters used in both constitutive models. 40
4.4 Input parameters in M-C model for the clay layer. 41
4.5 MCC stiffness parameters for the clay layer. 41
4.6 Construction phases for the simple pile model, scenario 1. 44
4.7 Construction phases for scenarios 2 and 3 corresponding to Brf. Sydney and in reversed construction order. 44
4.8 Varied parameter values for the parametric study. 44
4.9 Scenario 4: Parametric study sequence 45

5.1 Dates of installation of piezometers. 47
5.2 Time (in days) corresponding to the time factors displayed in the results. 54

1

Introduction

This chapter presents a brief background to the study of this thesis. The aim, objectives, and limitations of the study will be presented.

1.1 Background

With urbanisation bringing a predicted increase of population to cities, some challenges arise in how this influx of people should be accommodated. One way of meeting these challenges is through the densification of already exploited land in a city. The Swedish city of Gothenburg, partly employs this tactic of densification, as stated in the comprehensive plan developed by the municipality (Göteborgs Stad, 2022).

An area in Gothenburg known as Masthuggskajen is currently being redeveloped into a more densified area with several buildings having already been constructed (Göteborgs Stad, 2018). One building that is to be completed in the near future, as part of the redevelopment of Masthuggskajen is Brf. Sydney, which is a multistory apartment building with an underlying basement currently under construction by Skanska AB (Skanska, 2022a). The soil at Brf. Sydney consists mainly of soft clay to an approximate depth of 100 meter. Therefore, a deep foundation was needed to stabilise the ground of the upcoming building, consisting of cohesive piles, and a slab constructed on top. To be able to analyse the soil response during and following the construction of the foundation, five piezometers were installed at different depth to measure pore water pressure.

Excavating in soft clay with low permeability, as performed at Brf. Sydney, often results in heave which if restrained causes the bottom slab to experience pressure from below (Tornborg, 2017). This pressure needs to be accounted for when designing the slab, possibly resulting in extra reinforcement. This effect arises from the unloading process that results in negative excess pore pressure, which as they dissipate causes the soil to heave, comparable to how a compressed wet sponge expands when relieved of a surcharge load. Piling however, produces the opposite effect, generating positive excess pore pressure (e.g Isaksson, 2022). In short, excavation generates negative excess pore pressures, and piling generates positive excess pore pressures.

This report will compare the pore pressure evolution in soil, caused by different procedures of constructing the foundation of a building, with similar ground conditions to Brf. Sydney. In general, there are two procedures, either excavating before, or after the piles have been driven into the ground. If the increase in excess pore pressure when pilling, and the decrease of excess pore pressure when excavating, counteracts each other, the time-dependent heave effect on the slab could potentially decrease. This could ultimately lead to a more optimal design of the slab in terms of material use and its environmental impact.

1.2 Aim and Objectives

This thesis will study the combined impact pile driving and excavation processes have on the development and evolution of excess pore pressure, heave, and heave pressure.

The main objectives of the project which helps to address the aim, are described as follows:

- A literature study will be performed to support the interpretation and analysis of the data. Previous research on unloading and mass displacement in soft soil, coupled with pore pressure generation with regards to piling, will be used to design the methodology of the report.

- A collection of time-dependent pore pressure data from a site will be collected and aligned with the production time plan of the excavation and piling stages. This is done to observe how the pore pressure reacts to the different construction steps.

- Two numerical models will be created, one representing the pile installation and the other the excavation. These two models will be validated against existing literature to confirm that their behavior is in agreement with theory.

- Following the previous objective, a model will be constructed consisting of piling and excavation. The order of these processes will be switched to study the effects of piling before or after excavation, on heave of excavation bottom.

- A parametric study will be performed to generalise the result, with respect to varying permeability and soil stiffness.

1.3 Limitations

Limitations and external impacts of the project that will not be considered are described below:

- Only the pore pressure changes during excavation and piling will be analysed, not how it is affected by the load of the superstructure on the foundation.
- The influence of the previously constructed buildings in the area is not taken into account, nor are any future constructions.
- The numerical analyses are limited to a unit cell containing one pile
- The interface between the pile and soil will not be considered. Only the effects of the pile installation will be considered, since no pile element will be modeled.
- Any retaining structures part of the construction, such as sheet pile walls and struts, will not be considered.

2
Theory

In this chapter, the theoretical behaviour of the excess pore pressure during unloading (excavation) and mass displacement from driven piles will be presented.

2.1 Pore pressure change in low permeable soils

The soil can be either a three-phase material or a two-phase material, depending on whether it's dry (air and grains), fully saturated (water and grains), or partly saturated (water, grains, air) (Sällfors, 2013). When applying a vertical load onto a aqueous two-phase material, the stresses are carried by both the soil skeleton and the water. According to Terzaghis principle, the total stress is described as the sum of the effective stress and the pore pressure, see Equation 2.1. However, as water does not shear, this only applies to normal stresses and not shear stresses (Verruijt, 2017). The effective shear stresses are therefore equal to the total shear stresses (Bentley, 2023a).

$$\sigma = \sigma' + u \tag{2.1}$$

When applying or removing a load the response of the soil depends mainly on its permeability and drainage ability. If the soil has a low permeability the grains are small and therefore also the voids in between the grains (Knappett and Craig, 2012). Therefore low permeable soil does not drain as quickly as high permeable soil. The response of a low permeable soil to an applied load will consequently have an initial undrained response.

As previously mentioned, the soil can be either a three-phase material or a two-phase material, where the stresses generated by an applied load are carried by both the soil skeleton and the water in the voids (Sällfors, 2013). The pore pressure consists of a static/ steady state pore water pressure, u_s and an excess pore water pressure, u_e see Equation 2.2 (Knappett and Craig, 2012). When a vertical stress is applied to soil of low permeability and the lateral strain is assumed to be zero, the grains in the soil try to change position, but if the soil is fully saturated and the water is incompressible, the pore water needs to dissipate for this to occur. In low permeable soil, it takes time for the pore water to dissipate through seepage, resulting in an undrained short term response and an equal increase in total and vertical stress. However, in reality the lateral strain would probably not be equal to zero, resulting in an increase of the effective stress as well.

$$u = u_s + u_e \tag{2.2}$$

The change in pore water pressure creates a gradient and the water will continue to dissipate until the soil is fully drained and $u = u_s$, the increase in total vertical stress will be carried by the soil skeleton(Knappett and Craig, 2012). The deformation that occurs when the water dissipates and the soil skeleton rearranges is occurs during a process reffered to as consolidation. Compared to loading the soil, unloading, reduces the total stress and the excess pore pressure will be negative.

2.2 Compressibility and consolidation

As previously stated, the dissipation of excess pore pressures and the associated deformation is referred to as consolidation. The degree of this behaviour is partly governed by the load history of the soil (Knappett and Craig, 2012). The apparent maximum vertical load a soil has endured can be characterised by the apparent pre-consolidation pressure σ'_c. This can vary significantly depending on location, since it is determined by the geological, and anthropogenic loading history of the soil. How the soil will deform when subjected to a "new" load, will be governed to a large extent by whether the effective vertical stress in the soil, exceeds the apparent pre-consolidation pressure. If the effective stress generated by a "new" load $(\Delta\sigma + \sigma'_0)$ is less than the pre-consolidation pressure, i.e. $\sigma'_c > (\Delta\sigma + \sigma'_0)$, the soil will deform primarily elastically. Contrarily, when the pressure exceeds the preconsolidation pressure $\sigma'_c < (\Delta\sigma + \sigma'_0)$, the soil will consolidate resulting in viscoplastic deformations over time.

The ratio between the pre-consolidation pressure and the in situ vertical stress σ'_0 is known as the overconsolidation ratio, or $OCR = \sigma'_c/\sigma'_0$.

2.2.1 Compressibility

An important stiffness parameter to consider is the compression modulus M of the soil, which describes the relationship between compression and effective vertical stress (Larsson, 2008). Determined by the size of the difference between the vertical effective stress $(\Delta\sigma + \sigma'_0)$, and the pre-consolidation pressure σ'_c, the compression modulus of the soil will vary. For 1D-analysis, if $\sigma'_c > (\Delta\sigma + \sigma'_0)$, the oedometer stiffness can be described by M_0, which then characterise the elastic stiffness of the soil. If $\sigma'_c < (\Delta\sigma + \sigma'_0)$, the oedometer stiffness can be described by M_L, which characterise the plastic stiffness of the soil. Both M_0 and M_L are simplified linear stress-strain approximations.

M_0 and M_L is mainly assessed through CRS/ incremental loading oedometer tests where a soil sample is essentially subjected to increasing vertical stress, which causes it to compress and deform (Larsson, 1986). M_0 can be estimated through the empirical relationship $M_0 = 250c_{u,ref}$, where $c_{u,ref}$ is undrained shear strength. This originates from the fact that the initial modulus M_0 is typically too low compared to the actual in situ modulus of the soil due to sample disturbance. However, Larsson (1986) reports that $M_0 = 250c_{u,ref}$ is valid for soils with an OCR around 3. The empirical relationship for the compression modulus is actually dependent on both OCR, and c_u. For soils with an OCR in the interval 1 - 1.5, M_0 is in the range $400c_{u,ref} - 500c_{u,ref}$.

The compressibility of the soil can also be expressed in terms of swelling index κ and compression index λ(Muir Wood, 2004). These indices describe the relation between the change in void ratio and stress, where λ is the inclination of the virgin compression curve and κ is the inclination of the overconsolidated part of the curve, where Equation 2.3 can be used to calculate λ.

$$\lambda = \frac{1}{\ln(10)} \frac{\epsilon_2 - \epsilon_1}{\log(\sigma_2) - \log(\sigma_1)} \tag{2.3}$$

2.2.2 Time-dependent consolidation

The differential equation describing consolidation can be seen in Equation 2.4, and is described by Terzaghi (1943). Through the use of this equation the dissipation of excess pore pressures generated by a load, can be solved for at varying times. From this expression, it's evident that consolidation of excess pore pressures is governed by the permeability k, compression modulus M and the unit weight of water γ_w. These parameters are assumed to be constant in Terzaghis 1D consolidation theory, and can be grouped into the coefficient of consolidation c_v, as seen in Equation 2.5 (Knappett and Craig, 2012).

$$\frac{\partial u}{\partial t} = \frac{M}{\gamma_w} \frac{\partial}{\partial z} k \frac{\partial u}{\partial z} \tag{2.4}$$

$$c_v = \frac{kM}{\gamma_w} \tag{2.5}$$

2.3 Unloading and heave

The theory for swelling caused by unloading can be studied with the same theory as consolidation and loading (Persson, 2004). When soil is excavated, total stresses σ in the soil below the excavation are reduced (Kempfert and Gebreselassie, 2010). This happens because the soil has been relieved of weight previously posed by the layer above, which now has been excavated. The result of this is a reduction in pore water pressure u, rather than a corresponding change in effective stress σ'. This decrease in pressure generates a negative excess pore water pressure u_e, which in turn dissipates, i.e. $u_e \rightarrow 0$. When the negative excess pressure dissipates, the volume of the soil expands as water fills the pores. This results in heave of the soil under the excavation, akin to a "reverse consolidation" process. If a slab has been constructed on the excavation bottom, this heave can exert pressure on the slab from below. According to Persson (2004) the differential equation for heave caused by unloading, without accounting for creep, is defined in Equation 2.6.

$$\frac{\partial u}{\partial t} = \frac{M_{ul}}{\gamma_w}\frac{\partial}{\partial z}k\frac{\partial u}{\partial z} \tag{2.6}$$

Equation 2.6 is nearly identical to those found in Terzaghi (1943), with the difference being that the compression modulus is replaced with the unloading modulus. The equation describes how the dissipation of excess pore pressure is governed by the permeability of the soil k and the unloading modulus, without considering creep.

In Skempton (1954) the excess pore pressure due to unloading is described using Skempton's pore pressure coefficients, see Equation 2.7.

$$u_e = B\Delta\sigma_3 + A(\Delta\sigma_1 - \Delta\sigma_3) \tag{2.7}$$

where B = Pore pressure coefficient
A = Pore pressure coefficient
$\Delta\sigma_3$ = Minor principal stress
$\Delta\sigma_1$ = Major principal stress

The pore pressure coefficients can be determined from triaxial tests, where B relates to the minor principle stress as shown in Equation 2.8 (Skempton, 1954).

$$B = \frac{u_e}{\sigma_3} \tag{2.8}$$

When the soil is fully saturated, B equals 1, and for dry soil, B equals 0. The pore pressure coefficient A varies depending on the type of clay, as it relates to the change in deviatoric stress, $\Delta\sigma_1 - \Delta\sigma_3$ (Persson, 2004). According to Hansbo (1990), A tends to be within $0.5 - 1$ for normally-consolidated clay, and within $0 - 0.5$ for lightly over-consolidated clay. Hence, Persson (2004) writes that this implies that the change in porepressure can be equal to the change in vertical stress for one dimensional loading of an " *isotropic, linear elastic normally consolidated clay*". However, Skempton (1954) only presented values for A related to positive total stress increment as the data for a decrease in total stress was deemed insufficient. Also, as for unloading soil the stress change will be whit in the over-consolidated interval and $u_e \neq \sigma_v$ (Persson, 2004). Therefore, Persson (2004) refers to Equation 2.9 for unloading soil below the pre-consolidation pressure, where $u_e = \sigma_m$.

$$u_e = \frac{\Delta\sigma_v + 2\Delta\sigma_h}{3} \tag{2.9}$$

2.4 Heave pressure in soft clays

A study by Tornborg (2017) conducted for Skanska AB in conjunction with The Development Fund of the Swedish Construction Industry (SBUF), aimed to increase the knowledge across the industry regarding heave pressure and the governing processes. Furthermore, it aimed to support the industry in standardising how heave pressure can be accounted for, mainly when designing slabs. The study concluded that effective heave pressure, EHP against the bottom of a slab can be expressed as seen in Equation 2.10, where n is a heave pressure coefficient. The coefficient n is a function of the time passed between the excavation is finished and the slab is cast, as well as a function of the stiffness of the construction elements of the slab and the soil, as well as the permeability of the soil. In the report, it is stated that $n = 0.5$ can be considered a conservative approximation of the heave pressure. The report only studies the effect of unloading, the author therefore states that piles could have a preventing effect on the heave, as they act as reinforcement in the soil.

$$EHP = n \cdot \sigma'_{v0} \tag{2.10}$$

Where σ'_{vo} is the vertical effective stress at the excavation bottom level prior to construction.

2.5 Excess pore pressure due to pile driving

Pile driving in clay may often result in excess pore pressures in the vicinity of the pile (Hintze et al., 1997). When a displacement pile is driven into the ground, the zone closest to the pile becomes highly disturbed. The soil is displaced outwards from the pile, creating a zone radially from the center of the pile. This zone is referred to as the plastic zone, see Figure 2.1. Vesić (1972) derived an expression for the plastic zone which is seen in Equation 2.11. The expression is based on a cylindrical expansion of an infinite cavity with an internal pressure, under plane strain conditions.

$$\frac{r_{pl}}{r} = \sqrt{\frac{G}{\tau_{fu}}} = \sqrt{\frac{E}{2\tau_{fu}(1+\nu)}} \tag{2.11}$$

Where r_{pl} = Radial distance of the plastic zone from the center of the cavity
r = Radius of cavity
G = Shearing modulus of the soil
E = Young's modulus of the soil
ν = Poisson's ratio of the soil
τ_{fu} = Shear strength of soil in undrained conditions

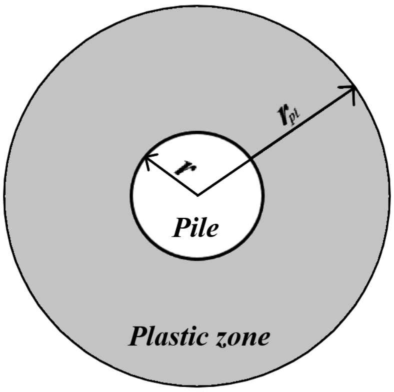

Figure 2.1: Illustration of the plastic zone around a pile represented by a cavity. Inspired by Hintze et al. (1997)

Before any pile is driven into the ground, the stresses acting in the ground are vertical effective stresses σ'_v, horizontal effective stresses σ'_h along with the pore pressure u_o. The vertical and horizontal stresses are the principal stresses at this state, where σ'_h equals $K_0\sigma'_v$. When a pile is driven into the soil, the radial stress becomes the major principal stress within the plastic zone (Lo and Stermac, 1965). As a result, the maximum excess pore pressure generated will then consist of two parts. the first part Δu_a, results from the change of ambient pressure, whereas the second part Δu_τ results from the shearing. Hence,

$$\begin{aligned} u_e &= \Delta u_\tau + \Delta u_a \\ &= [(1 - K_0) + (\Delta u/p)_{max}]\sigma'_h \end{aligned} \tag{2.12}$$

Where $(u_e/p)_{max}$ = Maximum excess pore pressure ratio
p = Consolidation pressure

Hintze et al. (1997) adds that Equation 2.12 by Lo and Stermac (1965) can be expressed in an alternate form seen in Equation 2.13. This expression, which is based on measurements obtained by Lo (1968), indicates that the maximum excess pore pressure increases with sensitivity of the clay. This is because the soil skeleton of a more sensitive clay will deform and collapse to a larger extent due to the disturbance caused by driving of the pile.

$$u_{e,max} = [(1 - K_0) + (0.5 + 0.267 \log S_t)]\sigma'_v \tag{2.13}$$

Where S_t = Sensitivity of the clay

2.5.1 Excess pore pressure gradient

How the excess pore pressure varies with distance from the pile is not particularly well-established, and can be expressed differently. One way of expressing it is proposed by Randolph and Wroth (1979) through Equation 2.14 which describes the excess pore pressure within the plastic zone. As can be seen in the expression, the excess pore pressure increases with undrained shear strength, and decreases with distance from the pile center within the plastic zone.

$$u_e = 2c_u \ln{(r_{pl}/r_x)} \tag{2.14}$$

Where u_e = Excess pore pressure due to pile driving
c_u = Undrained shear strength
r_x = Radial distance from pile center $r \leq r_x \leq r_{pl}$

A different expression for describing the excess pore pressure distribution around the pile is proposed by Pestana et al. (2002), see Equation 2.15, which is a modification of Vesić's (1972) work. Pestana et al. (2002) states that Equation 2.15 appears to yield an accurate estimate of the pore pressure ratio at different radial distances from the pile. Piezometer data collected during pile driving in silty clay and Equation 2.15 gives results that are in close agreement with the measured pore pressure ratios around the pile.

$$u_e/\sigma'_{vi} = r_{ueD}\sqrt{3r_0/(r_0+x)} \tag{2.15}$$

Where r_{ueD} = Pore pressure ratio at a distance of 1 pile diameter
r_0 = Radius of pile
x = Distance from pile wall

2.6 Dissipation of excess pore pressures

The excess pore pressures induced by pile driving will dissipate with time. The excess pore pressure will mainly dissipate radially from the pile, allowing for the soil to consolidate (Randolph and Wroth, 1979). Using cavity expansion theory Randolph and Wroth derived a set of equations which describes the process of consolidation around a driven pile, based on the pile represented as an expanding cavity in a soil medium. These equations have been solved and presented as a set of normalised curves for different stiffness ratios G/c_u. Figure 2.2, obtained from Randolph and Wroth (1979) displays the dissipation curves at the pile face for different ratios of G/c_u. c used in the normalised x-axes, is the coefficient of consolidation, assumed to be equal to c_v, and r_0 is the radius of the pile. These curves can be used to estimate the pore pressure at the pile face at different times after the pile has been driven.

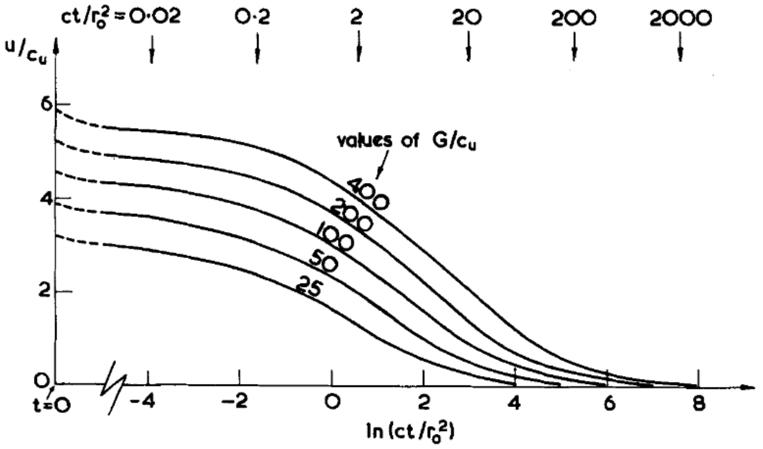

Figure 2.2: Variation of excess pore pressure at the pile face with time, from Randolph and Wroth (1979) (Permission for reuse granted by John Wiley & Sons (Wiley)).

The rate of dissipation will also vary radially from the pile. While initially the excess pore pressure are zero outside of the plastic zone, the dissipation results in non-zero excess pore pressures spreading to radii outside the plastic zone (Randolph and Wroth, 1979). Figure 2.3 depicts solutions to the equations by Randolph and Wroth for soil with $G/c_u = 50$. The curves correspond to different values of the time factor $T = (c_v \cdot t)/r_0^2$, which can be converted into an amount of time, where $c_v = kM_0/\gamma_w$ is the coefficient of consolidation. From the curves it can be derived that the excess pore pressure close to the pile drops rapidly just after driving. In a later article, Randolph (2003) presents results for $G/c_u = 100$, which can be seen in Figure 2.4. Both graphs follows a similar trend, with the latter one reaching a greater initial ratio $\Delta u/c_u$. Observe that the time factor curves are different between the graphs, making it difficult to directly compare dissipation between the two soil types. Baligh (1986) states that cavity expansion theory may overestimate the predicted excess pore pressures, due to not following the correct strain path. Baligh (1986) adds that for lightly over-consolidated soil, this error will be compensated for by ignoring excess pore pressure caused by the shearing of the clay.

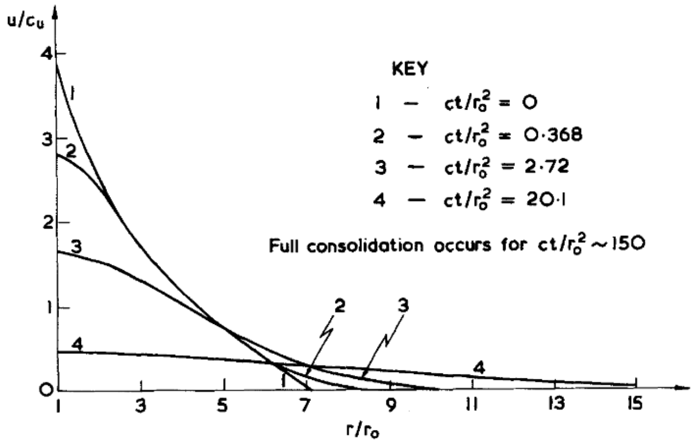

Figure 2.3: Variation of radial distribution of excess pore pressure with time after pile driving in soil with $G/c_u = 50$, from Randolph and Wroth (1979) (Permission for reuse granted by John Wiley & Sons (Wiley)).

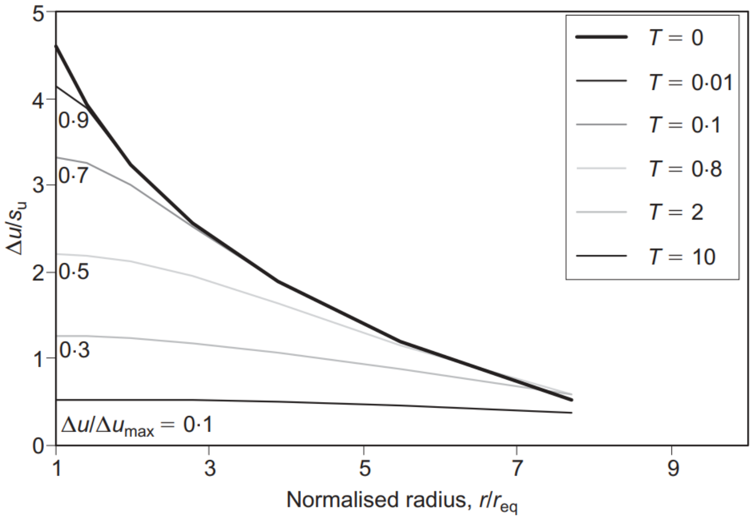

Figure 2.4: Variation of radial distribution of excess pore pressure with time after pile driving in soil with $G/c_u = 100$, from Randolph (2003).(Permission for reuse granted by Emerald Publishing Limited.

2.7 Numerical modelling

When modelling the behavior of the soil, different models can be used but each model will carry a varying degree of accuracy (Brinkgreve, 2005). Using a simple linear elastic model to analyse the behaviour of the soil might not capture its complexity due to its limitations. However, by using more advanced models, more parameters needs to be derived, requiring more soil test and assumptions from the responsible engineer. In the following subsections, important parameters, two constitutive models, and how they are implemented in the numerical analysis tool Plaxis 2D will be presented.

2.7.1 Geometry conditions for analyses

In Plaxis, either an axisymmetric or a plane strain model can be chosen to model the problem. The axisymmetric model is used for circular structures, where the y-axis represents the axial line of symmetry and the x-axis the radial distance (Bentley, 2023a). The model is solved in two dimensions as the circumferential direction has a thickness of zero. The model assumes a stress state that is identical in any angular direction as the cross-section has a uniform radial distance and load distribution.

The plane strain model is of infinite length. The displacements and strains are assumed to be zero in the out-of-plane directions, however, the normal stresses are taken into account (Bentley, 2023a). An example of a plane strain problem and an axisymmetrical can be seen in figure 2.5.

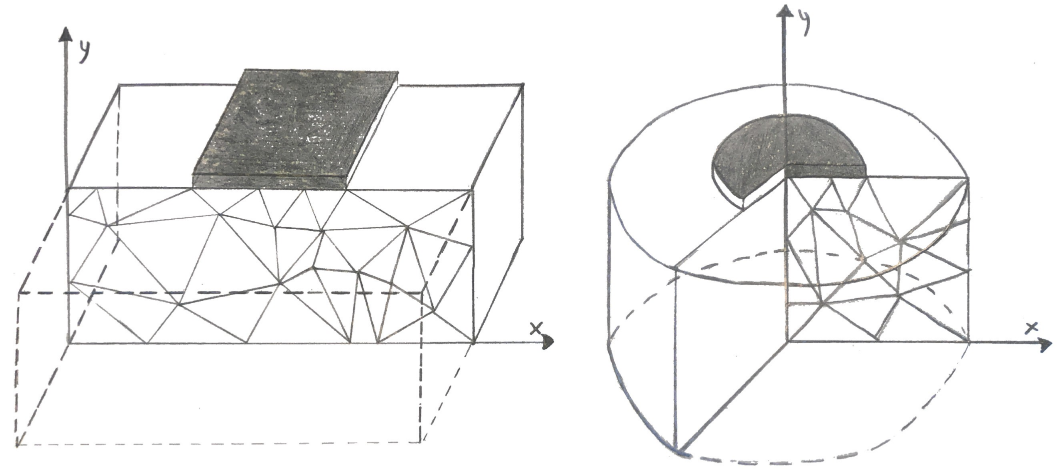

Figure 2.5: Examples of a plane strain (left) and axisymmetrical problem (right) (Inspired by Bentley (2023a)).

2.7.2 The Mohr-Coulomb model

Mohr-Coulomb is a linear elastic perfectly-plastic model that is normally used as a first approximation of the soil response (Bentley, 2023a). The model is partly based on Hooke's law of isotropic elasticity, and partly on Mohr-Coulomb failure criterion.

This is based on the fact that the strains consist of an elastic part (recoverable) and a plastic part (irrecoverable), see Equation 2.16 (Muir Wood, 2004). This means that the soil behaves linear elastic without sustaining any irrecoverable deformation up to a certain stress level, afterward the deformations are calculated assuming perfect plasticity Karstunen and Amavasai, 2017. It is the relation between stresses and strains that is described by Hooke's law, see Equation 2.17. Muir Wood (2004) writes that "*the elastic strain increment occurs whenever there is a change in stress (where the stress and strain are thought of as six-dimensional vectors)*". When the mobilized shear stress at any plane equals the shear strength, the soil starts to endure plastic deformations. The formula for critical shear stress can be seen in Equation 2.18.

$$\delta\varepsilon = \delta\varepsilon^e + \delta\varepsilon^p \tag{2.16}$$

$$\begin{bmatrix} \delta p' \\ \delta q \end{bmatrix} = \begin{bmatrix} K & 0 \\ 0 & 3G \end{bmatrix} \begin{bmatrix} \delta\varepsilon_p^e \\ \delta\varepsilon_p^e \end{bmatrix} \tag{2.17}$$

where p' = Mean effective stress
q = Deviatoric stress ($q = \sigma'_v - \sigma'_h$)
K = Bulk Modulus
G = Shear Modulus
$\delta\varepsilon_p^e$ = Incrimental elastic strain
$\delta\varepsilon_q^e$ = Incrimental elastic strain

$$\tau_f = c' + \sigma' tan\phi' \tag{2.18}$$

where c' = Effective cohesion
ϕ' = Effective friction angle

In Figure 2.6 Mohr's circle is presented. If the stress circle is inside the two tangent lines, no failure will occur, but if the circle touches the Coulomb yield surface, failure will occur (Verruijt, 2017). The yield surface can be described as an extension of Coulomb's formula of critical shear stress, see Equation 2.19, the model parameters used in the yield functions are the friction angle (ϕ') and the cohesion (c'). The yield function is derived from the Mohr-Coulomb circle using geometric relationships. If the yield function is $0 < F \leq 1$, the soil behaves elastically, if the yield function is $F = 0$, the soil is yielding. For the Mohr-Coulomb model, the yield surfaces create an irregular hexagon cone in the principal stress space, see Figure 2.7. These corners may cause problems during computation due to the fact that they are not continuous.

$$F = (\sigma'_1 - \sigma'_3) - (\sigma'_1 + \sigma'_3) sin\phi' - 2c' cos\phi' = 0 \tag{2.19}$$

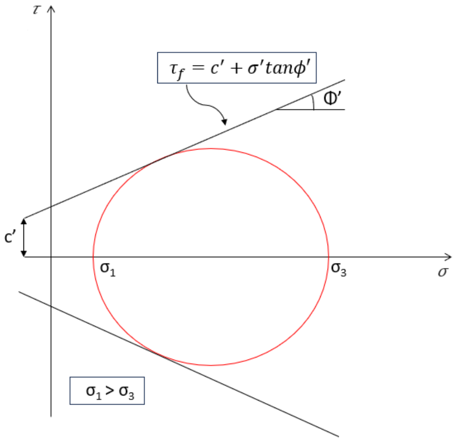

Figure 2.6: Mohr's circle, inspired by Verruijt (2017)

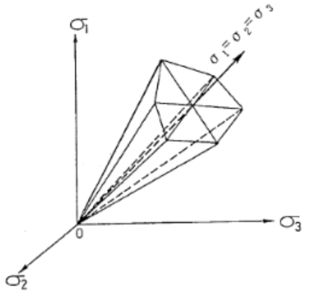

Figure 2.7: Mohr-Coulomb in principal stress space (retrieved from Sun et al. (2006)) (Permission for reuse granted by Elsevier).

The deformations when failure is reached assume perfect plasticity, and often non-associate flow rule, as associate flow rule can easily in the M-C model give negative normal strains (Karstunen and Amavasai, 2017). The flow rule for Mohr-Coulomb is defined through the dilatancy angle (ψ') of the soil, see Equation 2.20, which is also an extension of Coulomb's shear stress formula. The dilatancy angle is strongly dependent on the density of the soil, as sand usually have a higher dilatancy angle then clay.

$$G(\sigma') = \tau - \sigma_n' tan\psi' - const = 0 \tag{2.20}$$

The parameters required for the Mohr-Coulomb model in Plaxis 2D can be seen in Table 2.1. Instead of Young's modulus (E), the shear modulus (G), and the oedometer modulus (E_{oed}) can also be used.

Parameter	**Description**	**Unit**
E	Young's modulus	kN/m^2
ν	Poisson's ratio	-
c'	Cohesion	kN/m^2
ϕ'	Friction angle	°
ψ	Dilatancy angle	°

Table 2.1: Stiffness and strength parameters used by the M-C model in Plaxis 2D (Bentley, 2023a)

2.7.2.1 Limitations of Mohr-Coulomb model

The Mohr-Coulomb model is, as written in the beginning of this section, a first order approximation. Some of the limitations of the model are:

- Does not account for stress-dependency of stiffness (Bentley, 2023a). Usually as a soil is compressed the stiffness changes, but this is not taken into account in the Mohr-Coulomb model.

- Does not take time-dependent behavior as creep into consideration (Bentley, 2023a).

- Isotropic linear elastic behaviour gives unrealistic stress paths when simulating undrained behaviour.

2.7.3 Modified Cam Clay

The Modified Cam Clay model (MCC) is a soil model proposed by Roscoe and Burland (1968a), which is —as the name suggests— a modification of the Cam Clay model proposed by Schofield and Wroth (1968). What sets them apart is the shape and function that describes the yield surface, or yield locus as it's commonly referred to in literature (Muir Wood, 2004). Characterising these models are that they account for plastic deformation caused by compression, and that they incorporate a hardening response. This originates from the observed behaviour of clay during compression, which is the large change in volume that typically occurs when the stresses acting on the soil are increased in proportion. A large part of the resulting change in volume induced by this type of compression is irrecoverable (i.e. plastic). However, when a proportional stress path is applied to a Mohr-Coulomb model the response is elastic. (Proportional stress-path signifying the relationship between mean effective stress $p' = (\sigma'_v + 2\sigma'_h)/3$ and deviatoric stress $q = \sigma'_v - \sigma'_h$ is positive linear, i.e. the q over p' curve increases linearly.) The Cam Clay models provides an alternative to the Mohr-Coulomb model by incorporating this mechanism of plastic volumetric change during compression.

2.7.3.1 Elastic properties

The MCC model assumes that the soil possesses isotropic elastic behaviour, defined by the bulk modulus K and shear modulus G (Muir Wood, 2004). Additionally, the volumetric response of the soil can be expressed as:

$$v = v_k - \kappa \ln p' \tag{2.21}$$

Where κ is derived as the slope of the unload-reload line seen in figure 2.9, and v_k is a specific volume for a particular unloading-reloading relationship (Muir Wood, 2004). The incremental elastic strain relationship thus becomes:

$$\delta\varepsilon_p^e = -\frac{\delta v}{v} = \frac{\kappa}{v}\frac{\delta p'}{p'} \tag{2.22}$$

The bulk modulus K, a material property governing the volumetric decrease of a material under compression, can be expressed as in Equation 2.23 below. This suggests that K is not constant, but rather dependent on the stress level (Muir Wood, 2004)

$$K = \frac{\delta p'}{\delta\varepsilon_p^e} = \frac{vp'}{\kappa} \tag{2.23}$$

The incremental elastic strain relationship regarding deviatoric stress, for a constant shear modulus G, is then expressed as:

$$\delta\varepsilon_q^e = \frac{\delta q}{3G} \tag{2.24}$$

Following this, the elastic stiffness relationships can be expressed as follows:

$$\begin{bmatrix}\delta\varepsilon_p^e \\ \delta\varepsilon_q^e\end{bmatrix} = \begin{bmatrix}\kappa/vp' & 0 \\ 0 & 1/3G\end{bmatrix}\begin{bmatrix}\delta p' \\ \delta q\end{bmatrix} \tag{2.25}$$

2.7.3.2 Yield locus

As previously mentioned, the Cam Clay model (and MCC) defines a yield locus which determines whether a stress state will result in an purely elastic or elastic and plastic response. The yield locus is represented by a line, generating a shape within the $p' - q$ stress plane. In the case of the MCC model, the yield locus, illustrated in Figure 2.8, has the shape of an ellipse (Roscoe and Burland, 1968b). The actual yield function of the shape is defined in Equation 2.26. This function governs the behaviour of the soil at a certain stress state. If $f < 0$ the soil behaviour is elastic, whereas $f = 0$ results in yielding. Moreover, f is not allowed to exceed 0, instead the yield locus expands as the stress state "surpasses" the ellipse. The yield strength of the soil essentially increases if a stress state were to exceed the current yield strength. This behaviour is to a certain extent analogous to how the soil behaves with regards to consolidation.

$$f = \frac{q^2}{M^2} + p'(p' - p_p) \tag{2.26}$$

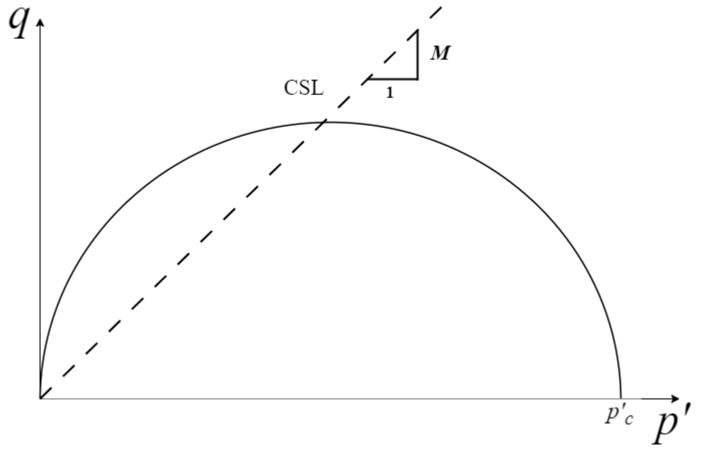

Figure 2.8: Yield locus of MCC model along with the Critical state line, based on Muir Wood (2004)

The Critical State Line (CSL), part of Figure 2.8, dictates the shear resistance of the soil.. This originates from the assumption of associated flow, which means that the plastic strain increment vector (shown in Equation 2.27) is constantly normal to the yield surface of the current state of stress (Muir Wood, 2004). The Critical State Line intersects the apex of all possible yield surfaces, which in combination with the aforementioned flow rule means that the plastic strain increment vector will always be vertical along this line, i.e. the horizontal (volumetric) component will be equal to zero. What this means regarding the behaviour of the soil, is that if the stress state reaches the apex of the yield locus the soil will deform, despite no variation in volumetric plastic strain ($\delta\varepsilon_p^p = 0; \delta p_c = 0$), in other words, critical state is reached meaning plastic shearing under condition of no change in volume or effective stress. Furthermore, the behaviour of the soil can be divided into a "dry side" and a "wet side" depending on whether the stress state lies left or right of the CSL. If the stress state is on the yield locus line, right from the CSL (wet side), the soil will compact (since $\delta\varepsilon_p^p > 0$) and harden ($\delta p_c > 0$) owing to the fact that the plastic strain incremental vector always is normal to the yield locus. Contrary on other side of the CSL (dry side) the soil will dilate and soften when the stress state is on the yield locus line ($\delta\varepsilon_p^p < 0$ and $\delta p_c < 0$) Roscoe and Burland, 1968b.

$$\begin{bmatrix} \delta\varepsilon_p^p \\ \delta\varepsilon_q^p \end{bmatrix} \tag{2.27}$$

In short, assume that the stress state is always on the yield surface in the following examples: When the stress state is right from CSL, the soil hardens and contracts as the yield locus expands. When the stress state is left from the CSL the soil softens and dilates, as the yield locus contracts. When the stress state reaches the CSL, the soil has reached critical state, i.e. shearing occurs under condition of no volume change or effective stress. If the stress state moves fully within the yield locus, the soil response is elastic.

2.7.3.3 Formulation in Plaxis

This part presents the formulations of the Modified Cam Clay model, which is relevant for use in Plaxis. Figure 2.9 depicts compression and unloading-reloading lines, typically obtained from the trend of the respective curves in an oedometer test (Muir Wood, 2004). The slopes of these lines are used to model the behaviour of the soil in the MCC model. The relationship between void ratio e and mean effective stress p' during virgin isotropic compression is expressed in Equation 2.28. λ is referred to as the isotropic compression index in the Plaxis Material Models Manual (Bentley, 2023a). This index describes the compressibility of the soil during primary loading. Equation 2.29 describes the relationship between void ratio and mean effective stress during the unloading-reloading phase, where κ is the isotropic swelling index. κ determines how the soil swells during unloading, and compresses during reloading until the stress state p_0 is reached once again, thereafter compressing in accordance with λ during further load. κ and λ are both used to describe the plastic compliance relationship, part of the *hardening rule*, described by Equation 2.30, which dictates how the size of the yield locus is dependent on the plastic volumetric strain.

$$e - e_0 = -\lambda \ln\left(\frac{p'}{p_0}\right) \tag{2.28}$$

$$e - e_0 = -\kappa \ln\left(\frac{p'}{p_0}\right) \tag{2.29}$$

Where
e_0 = Initial void ratio for loading/unloading
p_0 = Mean effective stress at start of unloading
λ = Compression index
κ = Swelling index

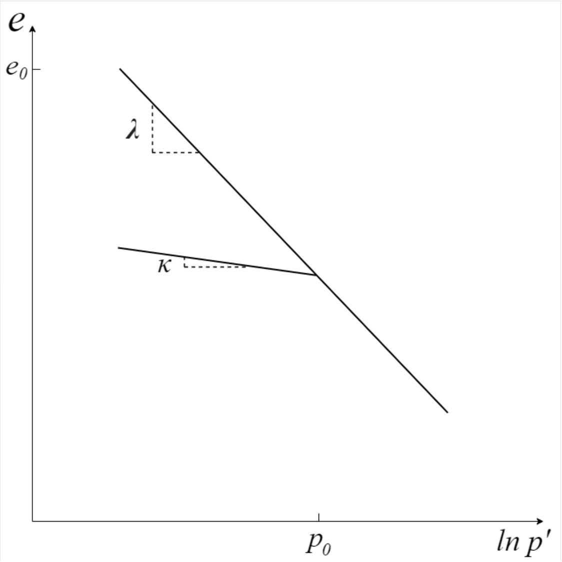

Figure 2.9: Compression and unloading-reloading lines, linear void ratio versus log mean effective stress, based on Muir Wood (2004)

$$\begin{bmatrix} \delta p'_0/\delta\varepsilon_p^p \\ \delta p'_0/\delta\varepsilon_q^p \end{bmatrix} = \begin{bmatrix} vp'_0/(\lambda-\kappa) \\ 0 \end{bmatrix} \tag{2.30}$$

The yield function in Plaxis is described as in Equation 2.26. Furthermore, the parameters required to apply the Modified Cam Clay model in Plaxis can be seen in Table 2.2.

Table 2.2: Parameters of the MCC model in Plaxis 2D (Bentley, 2023a)

Parameter	**Description**	**Unit**
λ	Cam-Clay compression index	-
κ	Cam-Clay swelling index	-
ν_{ur}	Poisson's ratio in elastic un-/reloading,	-
e_{init}	Initial void ratio for loading/unloading	-
M	Slope of CSL	-
K_0^{nc}	Coefficient of lateral stress in	-
	normal consolidation. Derived from M.	-

M can be obtained from the friction angle ϕ observed in triaxial tests, through different expressions depending on the stress state (Bentley, 2023a). Equations 2.31, 2.32, and 2.33 are used for triaxial compression, triaxial extension, and plane strain respectively. Additionally, M influences K_0^{nc} which in Plaxis is determined through the relationship seen in Equation 2.34. As a result of this, when M is chosen with regards to predicting the correct shearing strength, the value for K_0^{nc} becomes overestimated in normally consolidated conditions.

$$M = \frac{6\sin\phi}{3-\sin\phi} \tag{2.31}$$

$$M = \frac{6\sin\phi}{3+\sin\phi} \tag{2.32}$$

$$M = \sqrt{3}\sin\phi \tag{2.33}$$

$$M = \sqrt{\frac{(1-K_0^{nc})^2}{(1+2K_0^{nc})^2} + \frac{(1-K_0^{nc})(1-2\nu_{ur})(\lambda^*/\kappa^* - 1)}{(1-2K_0^{nc})(1-2\nu_{ur})\lambda^*/\kappa^* - (1-K_0^{nc})(1+\nu_{ur})}} \tag{2.34}$$

$$\text{Where} \qquad \begin{aligned} \lambda^* &= \lambda/(1+e) \\ \kappa^* &= \kappa/(1+e) \end{aligned}$$

2.7.3.4 Limitations of MCC

One limitation of this material model is that it doesn't account for creep deformations, which is when the soil deforms with time during constant stress (Knappett and Craig, 2012). There are other constitutive models which does account for this, thus requiring a creep related input parameter which brings further complexity to the model, as well as the spadework. Another thing to be weary about with regards to MCC, is that it can generate very large shear stresses when stress paths cross the critical state line (Bentley, 2023a). Additionally, the aforementioned softening behaviour seen during certain stress paths is also something to be cognizant of.

2.7.3.5 Cavity expansion and MCC

In a paper by Chen and Abousleiman (2012), a semi-analytical method was developed which models a gradual cavity expansion in a Modified Cam Clay soil. Results using this model indicate that the OCR of the soil has a strong influence on generated excess pore pressure around the cavity, both in terms of magnitude and the distribution. The results presented from using the method shows that the response of the soil is in compliance to results produced from a finite-element analysis of cavity expansion by Randolph et al. (1979), also using the Modified Cam Clay model. For a soil with an OCR of 1.2 the excess pore pressures and the distribution of which, showed significant similarities to the results of Randolph and Wroth (1979), shown in Figure 2.3.

2.7.4 Pore pressure definitions in Plaxis

In Plaxis, Terzhagi's principle (Equation 2.1) is developed further taking into account the saturation (S_{eff}) and the pore pressure coefficient (α_{biot}) resulting in Equation 2.35.

$$\sigma = \sigma' + \alpha_{biot} S_{eff} u_w \tag{2.35}$$

where α_{biot} = Biot's pore pressure coefficient
S_{eff} = Effective degree of saturation

When using the behaviors Undrained A or Undrained B in Plaxis, excess pore water pressure is generated during consolidation and plastic calculations (Bentley, 2023a). In (2023a) the pore pressure (u_w) is calculated as in Equation 2.2, where the total pore pressure is the sum of the static pore pressure (u_s) and the excess (u_e). The static pore pressure is given or calculated (if fully coupled), from the chosen groundwater level/ phreatic level, whereas the excess pore water pressure needs to be calculated (Bentley, 2023a). The excess pore pressure changes over time, therefore the derivative of the total pore pressure can be written as in Equation 2.36.

By using the inverted form of Hooke's law and multiplying the stiffness matrix with the effective stress in all directions (xx, yy, zz), an equation to calculate the rate of excess pore pressure change is generated (Equation 2.37). Also, when calculating the excess pore pressure in an effective stress calculation, a bulk modulus of water will be added to the stiffness matrix (Bentley, 2023b). In Equation 2.38 and 2.39 the compressibility for water respectively the solid material is presented, these are dependent on the bulk modulus for water respectively the solid material.

$$\dot{u}_w = \dot{u}_e \tag{2.36}$$

$$\dot{u}_e = \frac{\alpha_{biot} \dot{\varepsilon}_v}{n C_w + (\alpha_{biot} - n) C_s} \tag{2.37}$$

$$C_w = \frac{1}{K_w} \tag{2.38}$$

$$C_s = \frac{1}{K_s} \tag{2.39}$$

where C_{w} = Compressibility of water
C_{s} = Compressibility of soild
n = soil porosity

In Plaxis (2023a) equations for the undrained parmaters E_{u} and v_{u} are generated through Hooke's law. The inverted form of Hooke's law is used but with undrained parameters and in terms of total stress as opposed to effective stress. The equations can be seen below.

$$E_u = 2G(1 - v_u) \tag{2.40}$$

$$v_u = \frac{3v' + \alpha_{biot}B(1 - 2v')}{3 - \alpha_{biot}B(1 - 2v)} \tag{2.41}$$

$$B = \frac{\alpha_{biot}}{\alpha_{biot} + n(\frac{K'}{K_w} + \alpha_{biot} - 1)} \tag{2.42}$$

where B = Skempton's B parameter

The value for v_u is by default set to 0.495 making it compressible to a small degree, if v_u was set to 0.5 it would be fully incompressible but it would lead to a singularity of the stiffness matrix and undefined equations (Bentley, 2023a). In Plaxis they further explain that the bulk mudulus of water needs to be greater than the bulk modulus of the soil skeleton, to ensure this v' needs to be less or equal to 0.35.

The Biot's coefficient is equal to 1 for incompressible grains and less than 1 for compressible grains (Bentley, 2023a). The compressibility of the grains is normally disregarded as the compressibility of the soil skeleton is usually considerably higher. However, at great depths and under high pressure the stiffness of the soil skeleton becomes comparable to the stiffness of a single grain. The default value in Plaxis for α_{biot} is 1 for the undrained definition option but can be changed to values in the range of 0.001 and 1.

To summarise, there are different ways to obtain the excess pore pressure and it depends on how the bulk modulus is calculated. The different ways are:

- (*Biot effective stress concept)* Specifying K_w and α_{biot}.
- (*v-undrained definition- Skempton B based)* Specifying Skempton's B-parameter.
- (*v-undrained definition - Direct)* From Equation 2.43, when α_{biot} =1

$$\frac{K_w}{n} = \frac{3(v_u - v')}{(1 - 2v_u)(1 + v')}\ K' = \frac{0.495 - v'}{1 + v'}300K' \geq 30K' \tag{2.43}$$

3

Case study

Brf Sydney is being constructed as part of the new district Masthuggskajen in Gothenburg, Sweden. Together with several actors, Masthuggskajen is, at the time of writing, being redeveloped to contain housing, hotels social areas, and offices. Figure 3.1 illustrates the area of Masthuggskajen when completed. Number 18 in Figure 3.1 displays where Brf Sydney is currently under construction.

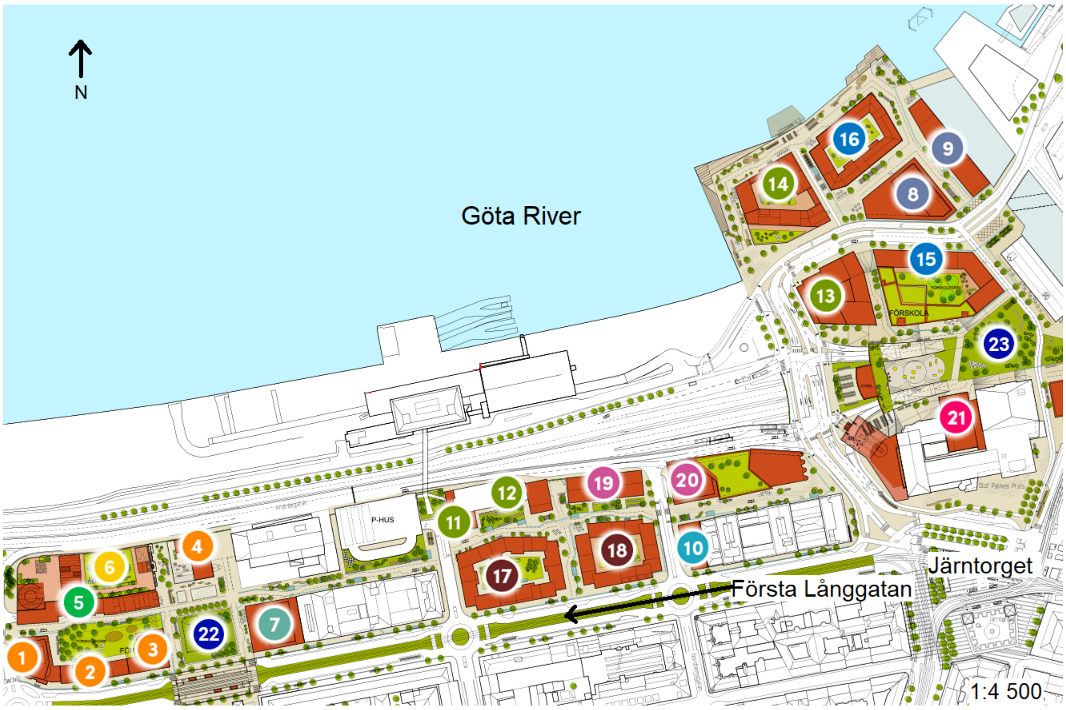

Figure 3.1: Overview of Masthuggskajen, Brf. Sydney is located at number 18 (retrieved from Masthuggskajen, 2024-01-24).

3.1 Soil Characteristics

The soil characteristics of the site are influenced by the areas loading history, as Masthuggskajen has historically been used as a wharf. Before the area was used as a wharf the shoreline was situated close to Första Långgatan (Schager, 2017), just south of Brf. Sydney. When constructing the wharf at the end of the 19th century, the area was filled with fill material, thus moving the shoreline north to where it is situated today. Therefore, at the end of the 19th century, the area in which Brf Sydney is situated was expanded and filled with fill material. The fill material consists of a mixture of sand, silt, gravel, clay, and brick remains (ELU Konsult AB, 2021). The thickness of the fill varies between 2-4 meters and the ground surface level in the area is approximately +2.0 m AMSL (Above Mean Sea Level), in reference system RH2000. The groundwater table is located at a level of approximately +0.5 m and is assumed to be hydrostatic, but as the site is close to Göta river the groundwater table is also affected by changes in water levels. Below the fill material, there is a clay layer of approximately 100 meters thickness that lies on top of a layer of friction soil on bedrock. (ELU Konsult AB, 2021). Near the site of Brf. Sydney the Göta tunnel is situated, which was studied in Tornborg et al.(2021), approximately located at number 23 in Figure 3.1. The authors write that the areas around the Göta River are mainly dominated by deep deposits of sensitive soft clays, which applies to Brf. Sydney. The study by Tornborg et al., benchmarked a rate-dependent constitutive model know as Creep-SCLAY1S, against measured data from an excavation as part of the construction of the Göta Tunnel in Gothenburg. Although the Göta Tunnel excavation was carried out under water, pore pressure data from this study might be useful as a tool for comparison with the pore pressure data.

In Table 3.1 the unit weight, and strength properties of the soil deposits at Brf. Sydney is presented. The values for the unit weight and strength properties in Table 3.1 are taken from the Geotechnical PM written by Skanska (2022b) for the design of slab, sheet pile wall, and piling foundation.

Table 3.1: Dimensions, unit weights, and strength parameters of the different soil layers, retrieved from Skanska (2022b)

Soil Layer	**Elevation [m]**	**Unit weight [kN/m^3]**	**Strength parameters**	
			ϕ[°]	**c$_u$[kPa]**
Fill	+2 to -2	$\gamma = 18, \gamma_s = 20$	36	
Clay 1	-2 to -3	$\gamma = \gamma_s = 15.5$	30	17.5
Clay 2	-3 to -8	$\gamma = 16.5$	30	17.5
Clay 3	-8 to -20	$\gamma = 16.5$	30	24 + 0.4z*
Clay 4	-20 to -40	$\gamma = 16.5$	30	28.8 + 1.6z*
Clay 5	-40 to -100	$\gamma = 16.5$	30	60.8+1.6z*

3.2 Pore pressure sensors

Five PVT direct push piezometers (Geotech AB, 2024) with built-in data loggers were installed in the center of the site pre-construction at depths of 5, 10, 15, 20, and 40 meters. The approximate position of the piezometers is illustrated in Figure 3.2. The piezometers were installed to measure the pore water pressure during construction, but they will not be removed after construction, enabling future research. Through the fill material, a casing pipe was used to protect the piezometers, the soil was pre-drilled to 20 cm above the final placement of each device. The piezometers were then pressed down to their respective depths, for the tip to end up in undisturbed material. The cables are protected with 1" pipes. The piezometers log data two times a day, once at midnight and once at noon.

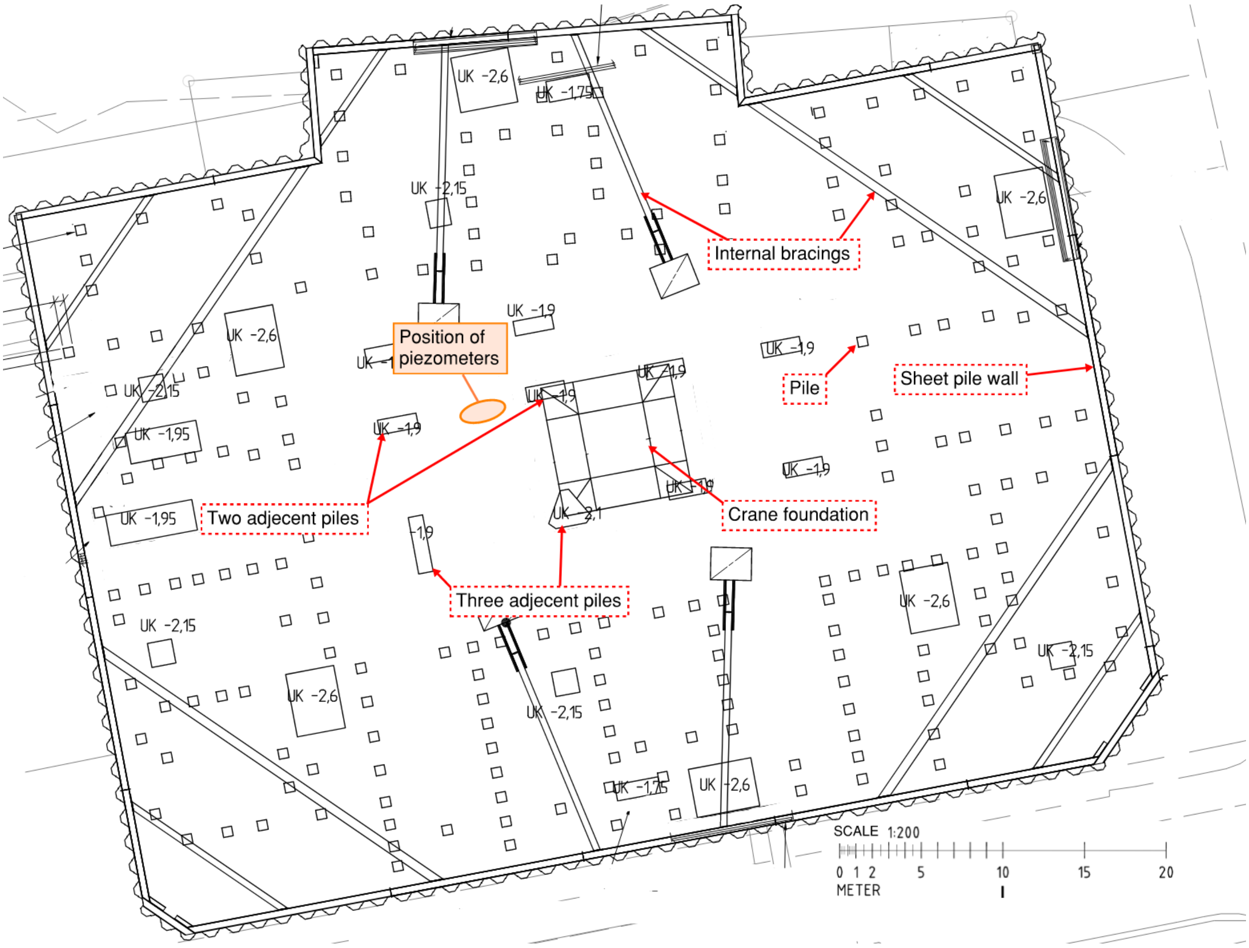

Figure 3.2: Position of the piezometers within the construction site (modified technical drawing, G-15-1-0001 (Skanska Teknik, 2023).

3.3 Construction process

The construction of Brf. Syndney's foundation was done as follows; Firstly, the whole site was excavated from elevation +2 m to +0.6 m, during the period between 2023-03-03 and 2023-03-31 (Jansson, 2024). Secondly, an excavation was carried out sequentially in parts, down to elevation -1.8 m. The excavation was done in this manner to allow for the installation of struts at the corners of the site. Afterward, a layer of blinding concrete was cast on the excavation bottom, on which the construction vehicles could safely operate. Finally, pre-casted concrete piles were driven through pre-casted holes in the blinding concrete slab.

3.3.1 Excavation process

As mentioned before, the whole site was first excavated from +2 m down to +0.6 m AMSL. This was the maximum depth that could be excavated before struts and bracers were required for stability. Following this excavation, the site was divided into zones where excavation was performed in conjunction with strut installation between different dates. Figure 3.3 displays information regarding the division of the excavation zones as well as the dates in which the excavation was carried out (Jansson, 2024).

Shortly after each zone was excavated, a 20 cm thick slab of blinding concrete was cast, on top of an approximately 10 cm thick macadam layer. The arrows in Figure 3.3 represent the direction of each excavation, which was done with regard to the installation of the struts. At the corner zones, the inner strut was installed first then followed by the outer strut. Furthermore, the north (N) and south (S) zone had inclined struts installed between the sheet pile wall and the blinding concrete slab. As a result of archaeological findings uncovered during the excavation, the excavation process was prolonged and the piling was postponed.

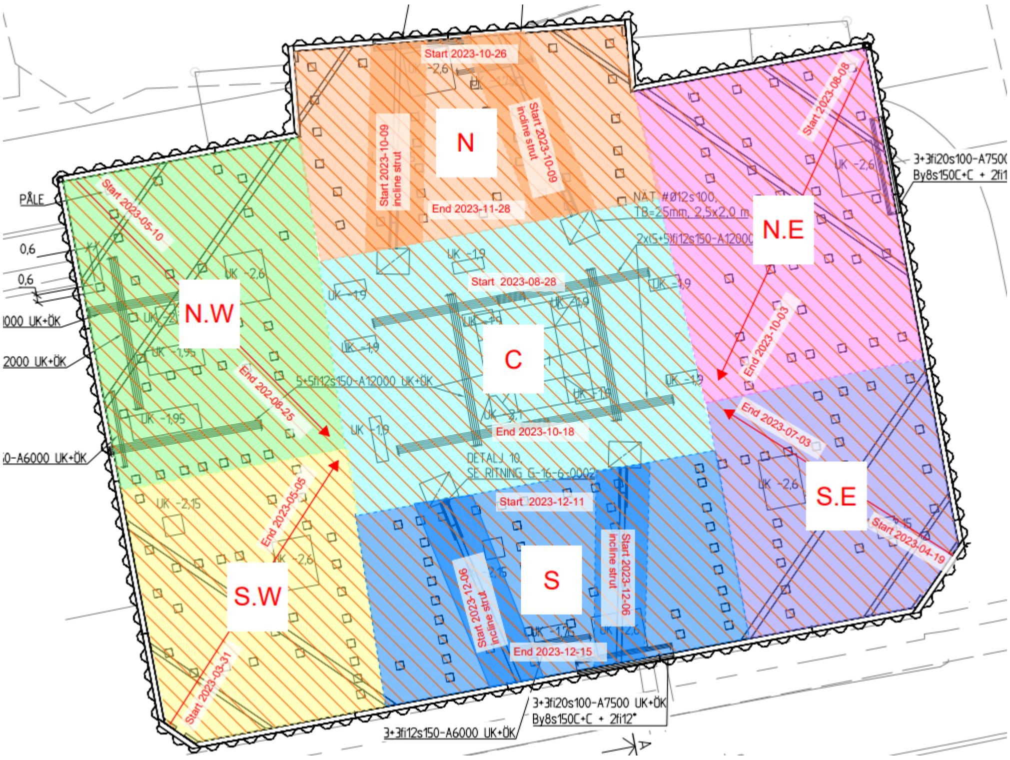

Figure 3.3: Partition of zones during second excavation phase (from +0.6 m to -1.8 m), with dates of respective excavation span (modified technical drawing, G-15-1-0001 (Skanska Teknik, 2023)).

3.3.2 Piling process

To enable the pilling equipment to work safely from the excavation bottom blinding concrete was cast and holes were prepared in the slab in which the piles would be driven. The foundation consisted of 246 piles, the piling process started on 2023-14-12 and progressed through the winter and early spring of 2024. Before each pile was driven into the ground, the pile locations was pre-augered to a depth of 15 m. In Figure 3.4 the timeline of the pile installation can be seen. After all the piles had been installed, rebar and form works commenced and then the 0.45 m thick slab was cast.

The foundation is built on three different types of piles, the piles are all 57 meters long and have the same dimensions. Type 1 and type 2 make up approximately 90 % of the 246 piles, the 57 meter long piles consist of three concrete piles of 14 meters each and one timber pile of 15 meters. The concrete piles are squared with the dimension of 270x270 mm^2 and the timber pile is circular with an increasing radius of Ø = 170+12 mm/m. The difference between type 1 and type 2 is in the class of strength of the concrete elements, type 1 has a strength of C50/60, and type 2 of C60/75, type 2 piles are designed with a higher class of strength. Type 3 has the same dimension and strength as type 1, but for type 3 the rebar is attached to the slab. Pile type 3 acts as tension piles designed to counteract uplifting forces, generated by water pressure and restrained heave before the slab is fully loaded by the superstructure

Figure 3.4: Pile installation reported per week at Brf. Sydney, the figure was generated with knowledge from propile about installation dates and the technical drawing, K-15-1-0080 .

4

Method

The methodology used in this thesis consisted of three parts. In the first part, the measured pore water pressure data and the production stages at Brf. Sydney was compiled into a timeline. In part two, two analytical methods were used to analyse how unloading and piling, separately, affect the excess pore pressure in clay. To make sure that the model behavior is consistent with the theory with regards to piling and unloading, the numerical model was validated against the analytical results. (The excess pore pressure with regards to piling was validated against analytical calculations and the unloading behavior was validated against consolidation theory, both of which are thoroughly explained in later sections.) In the final part, a 2D numerical finite element model was constructed which consisted of multiple steps to simulate the whole construction sequence of the foundation. A parametric study was performed, using a FE-model, to study how varying the construction order and parameters affect the results.

4.1 Pore pressure data, Brf. Sydney

The timeline of the excavation was retrieved from a supervisor at Brf. Sydney, this was compiled and plotted with the corresponding pore pressure data. To establish a timeline for the pile installation the software *Propile* was used.

The collected pore pressure data were given in the form of mH_2O, which was converted to kPa. The density of the water was set to 1012.5 kg/m^3 in the calculation because of its proximity to Göta River indicating a higher level of salinity. The static pore pressures were calculated by assuming a groundwater level at +0.5 m, with hydrostatic increase with depth. This was then used to calculate the excess pore pressure. The piezometers did not log the corresponding atmospheric pressure, instead the data were collected from SMHI (Swedens Meterological and Hydrological Institute). An average value of the atmospheric pressure was chosen since correcting for measured pressure values for each date introduced more noise and fluctuations in the corrected pore pressures. Rain data were also retrieved from SMHI and compared to the pore pressure data, this did not indicate a correlation and was thus not investigated further.

4.2 Analytical calculations

This section describes the procedure of the analytical calculations of pore pressure during the two construction stages, excavation and piling. Excess pore pressures were analysed separately for each construction stage. The reason for this is that reasonable empirical or analytical methods concerning the combined effect of unloading and piling have been difficult to obtain, hence no combined analytical analysis of both excavating and piling have been conducted. The results of these calculations were compared against the results produced in the numerical model (see section 5.2 and 5.3). The depths chosen for the analytical calculations correspond to the depths at which the piezometers are located in the soil under Brf. Sydney.

4.2.1 Negative excess pore pressures due to unloading

The negative excess pore pressure when the soil is unloaded during excavation was calculated using Equation 2.7. To use this equation, the extent of how each excavation contributes to unloading the soil had to be calculated. This was done using Equation 4.1 found in Alén (1998), which is based on Boussinesq's approximation of the distribution of stresses in soil generated by a load. This equation was used to calculate the difference in vertical stress, that each excavation stage contributes with. A negative load corresponding to the unloading caused by the excavated soil was used as input for the equation.

$$\begin{aligned}\Delta\sigma_v(x,y,z) = \frac{p}{\pi^2}\cdot &\left[\left[\frac{2z(B+2x)}{4z^2+(B+2x)^2}+\arctan\left(\frac{B+2x}{2z}\right)\right]+\right.\\ &\left.\left[\frac{2z(B-2x)}{4z^2+(B-2x)^2}+\arctan\left(\frac{B-2x}{2z}\right)\right]\right]\cdot\\ &\left[\left[\frac{2z(L+2y)}{4z^2+(L+2y)^2}+\arctan\left(\frac{L+2y}{2z}\right)\right]+\right.\\ &\left.\left[\frac{2z(L-2y)}{4z^2+(L-2y)^2}+\arctan\left(\frac{L-2y}{2z}\right)\right]\right]\end{aligned} \tag{4.1}$$

Where p = Surcharge evenly distributed on an area
B = Width of area
L = Length of Area

To calculate the load spread, a coordinate system was derived, where the position of the piezometers was assumed as the origin. Furthermore, the zones seen in Figure 3.3 were converted into negative uniform loads, acting within each excavation zone. How each zone contributes to unloading the soil at the point and depth of each piezometer could then be assessed. With $\Delta\sigma_1$ known, $\Delta\sigma_3$ was calculated using Equation 4.2. Where *const.* is a constant describing the relationship between $\Delta\sigma_3/\Delta\sigma_1$. This constant was obtained usin Hansbo (1990), and equal to 0.2 in this case. After calculating the contribution in negative excess pore pressure of each excavation, they were then summarized and plotted against the days each excavation lasted. This resulted in a potential maximum negative excess pore pressure at different times during the excavation process. Therefore, this calculation does not take into account the consolidation of the negative excess pore pressures, which starts as soon as the area is excavated. The depths chosen for these analyses correspond to depths where piezometers are located.

$$\Delta\sigma_3 = \Delta\sigma_1 \cdot const. \tag{4.2}$$

4.2.2 Excess pore pressures due to piling

Initial excess pore pressures due to pile installation were calculated using the expression proposed by Randolph and Wroth (1979), which is explained in the following section. Furthermore, using graphs developed by Randolph (1979, 2003) variation of excess pore pressure around one pile could be determined.

4.2.2.1 Initial excess pore pressure distribution

The initial pore pressure distribution around a pile after driving was calculated using equation 2.14 by (Randolph and Wroth, 1979). Equation 4.3 from Vesić (1972), was used to determine the radius of the plastic zone r_{pl}.

$$r_{pl} = r_0\sqrt{\frac{G}{c_u}} \tag{4.3}$$

Where u_e = Excess pore pressure due to pile driving
c_u = Undrained shear strength
r_x = Radial distance from pile center $r \leq r_x \leq r_{pl}$

To calculate the initial pore pressure distribution, both the shear modulus G and undrained shear strength c_u are required. The undrained shear strength c_u for the different depths are seen in Table 4.1. Using the approximation that $M_0 \approx 500c_u$ (see Section 2.2.1), along with the relationships in Equation 4.4 and 4.5, all of which were obtained from Larsson (2008), G could be determined. Poisson's ratio ν was chosen to be equal to 0.2.

Table 4.1: Undrained shear strengths c_u at each respective depth used in the analytical calculations. Values retrieved from Skanska (2022a).

Level [m]	c_u **[kPa]**
-18	28
-38	57.6
-43	65.6

$$M = \frac{E(1-\nu)}{(1+\nu)(1-2\nu)} \tag{4.4}$$

$$G = \frac{E}{2(1+\nu)} \tag{4.5}$$

The excess pore pressure variation with radial distance from the pile was then calculated according to Equation 4.6, obtained from (Randolph and Wroth (1979)).

$$u_e = 2c_u \ln\left(r_{pl}/r_x\right) \tag{4.6}$$

4.2.2.2 Excess pore pressure variation at pile face

The following procedure was performed for different depths, to calculate the variation of excess pore pressure at the pile face with time. First, the stiffness ratio G/c_u at the corresponding depth was calculated. Using the empirical approximation that $M_0 \approx 500c_u$, with the relationships in Equation 4.4 and 4.5, the stiffness ratio G/c_u becomes constant with depth and equal to 187.5.
Having obtained the stiffness ratio, points just under the curve corresponding to a stiffness ratio $G/c_u = 200$ (found in Figure 2.2) were extracted using a web-based tool called Plot Digitizer. These points were then exported in a CSV-file for further calculations using Python. In Figure 2.2, the x-axis is based on the time factor T and the y-axis is expressed in the ratio $\Delta u/c_u$. The equation for the time factor T can be seen in Equation 4.8 (Randolph and Wroth, 1979). Important to note is that c_v is the coefficient of consolidation in the vertical direction, and that the consolidation of excess pore pressures around the pile likely occurs in the horisontal direction. However, Randolph and Wroth (1979) states that that c can be assumed to be equal to c_v, since at large radii the radial consolidation resembles that of one-dimensional consolidation. Hence, c_v was determined using Equation 4.7, where $M = M_0$ and k was assumed equal to 10^-9 m/s which is typical for clays in Sweden (Larsson, 2008)). γ_w was assumed equal to 10.125 kg/m^3 (see section 4.1). A Python script was created that read the data points from the CSV-file and converted them from the normalised axes seen in Figure 2.2, into a plot of excess pore pressure variation with time expressed in days.

$$c_v = \frac{kM}{\gamma_w} \tag{4.7}$$

$$T = \frac{c_v t}{r_0^2} \tag{4.8}$$

Where c_v = Coefficient of consolidation
r_0 = Radius of pile
t = Time

4.3 Numerical modeling

For the numerical analysis in this work the software Plaxis 2D, version 2201 was used. This section describes how the numerical model was constructed and run. The model was kept simple (a unified clay layer was assumed and no retaining structures were taken into account) throughout the analysis to aid comparison to analytical results and add complexity successively. Two different material models were used to investigate the impact of the modelled soil response; Mohr-Coulomb (M-C), and Modified Cam Clay (MCC).

The methodology for the numerical modeling was structured as below:

1. A simple "pile model" without the excavation was created, where the excess pore pressure due to pile installation were validated against Randolph (2003, 1979).
2. A simple unloading model was created without the pile installation, where the consolidation of excess pore pressure after excavation were validate against Terzaghis solution for 1-dimensional consolidation.
3. The two models were merged into one model with the construction sequence and timeline for Brf. Sydney being used.
4. The construction order was reversed, the resulting heave and pore pressure evolution were compared to the original order of construction.
5. A parametric study was conducted where the permeability and stiffness were varied.

4.3.1 Geometry and boundary conditions

The main interest when conducting the numerical modeling were the pore pressure evolution. An axisymmetrical model was created, to idealise and not account for the supporting structures when conducting the analysis. Two models with different geometry, one to simulate the pile installation and the other the excavation order, were used.

To verify if the pile installation response in the numerical model equates to the theory of Randolph (see section 2.6) a simple pile installation model was created. The 57 meter pile was simulated as a cavity expansion, with an exception of the first 15 meter where the soil had been removed by pre-augering. The pile installation was simulated using a 100% volumetric expansion in the cluster corresponding to the pile, as the piles in reality are rectangular the equivalent radius of the pile was calculated using; $r_{pl} = b/\sqrt{\pi}$, where b is the width of the square pile. This was based on a geometrical relationship assuming an equal cross-sectional area between the two shapes. With $b = 0.27$ m (see subsection 3.3.2), r_{pl} became equal to 0.21 m The right boundary of the model was decided to be 30 meters from the pile centre, as according to Randolph and Wroth (1979) the pore pressure is unchanged at this distance. This originates from the boundary condition which is that $u_e \rightarrow 0$ as $r \rightarrow \infty$ for $t \geq 0$ (Randolph and Wroth, 1979). This is simplified by introducing a radius r^*, beyond which the excess pore pressures always will be negligibly small, and can be ignored for radii beyond r^* (i.e. $u_e = 0$ for $r > r^*$). Randolph and Wroth (1979) states that r^* can be expected to be within the interval $5 - 10r_{pl}$, where the larger end of the interval was chosen as the boundary for this analysis. Mentioned in chapter 2, cavity expansion is a common method to analyse pore pressure build-up during piling. This method is based on expanding a cylindrical cavity in a elasto-plastic material. The pile, modeled as a cylinder thus becomes a circular type pile. This keeps the numerical model consistent with the theory, making comparisons of results more applicable.

The excess pore pressure variation from the simple pile model was compared against the analytical results obtained through theory found in Randolph and Wroth (1979). Comparisons were also made to the radial variation of excess pore pressures at different times seen in Figures 2.3 and 2.4, though no direct comparisons could be made since the graphs in these figures only apply to soil with stiffness ratios $G/c_u = 50$ and 100, whereas the stiffness ratio for the model equals to 187.5. Nevertheless, a comparison of the general time-dependent response was still made to see whether the pile simulation in the numerical model deviates heavily from the time-dependent response found in the analytical solutions. The response of the Mohr-Coloumb as well as the Modified Cam Clay, were simulated in this simple pile model and compared against theory and each other.

The second model that was designed as a unit cell, representing the red circle shown in Figure 4.1. The unit cell had a radial distance of 6.5 meters, the radius equals the average distance of the closest surrounding piles. The location of the unit cell was chosen as it is located in a piling area and the piezometers are inside the radial distance. The geometry of the model can be seen in Figure 4.2, the depth of the model (y_{min}) was set to 100 meters, with open groundwater flow boundaries at the top and bottom as the clay rests on a layer of friction soil. For this model, only the excavation was first analysed to validate it against Terzaghis solution for one-dimensional consolidation. Thereafter, both the pile installation and excavation were simulated in the same model.

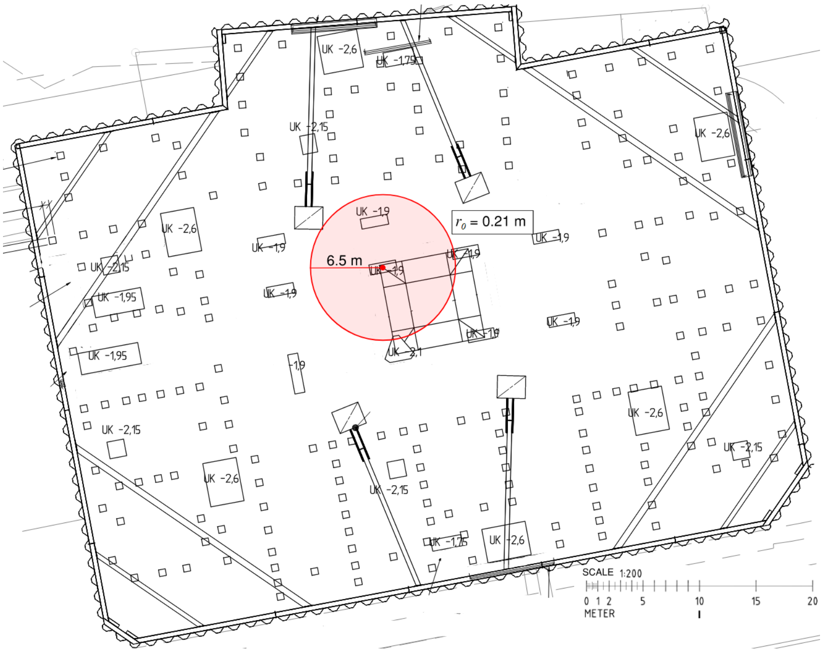

Figure 4.1: Location of the simulated unit cell. (Modified technical drawing, K-15-1-0001 (Skanska Teknik, 2023).

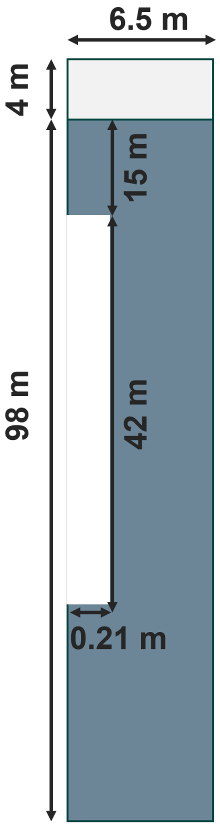

Figure 4.2: Geometry of numerical model corresponding to unit cell in Figure 4.1 (not to scale).

The hydraulic and mechanical boundary conditions can be seen in Table 4.2, where the left hydraulic boundary was assumed to be closed and normally fixed to fulfill symmetry in both models. The right hydraulic boundary in the simple pile model was assumed to be open (width of 30 m), as according to Randolph (1979) the pore pressure should be unchanged at such a radial distance from the pile. However, for the second model, the right hydraulic boundary was assumed to be closed as it simulated a unit cell. (A closer right boundary could also simulate a more representative response in contrast to an open boundary, as the pile in reality is surrounded by additional piles). The vertical boundaries were set to be normally fixed to allow vertical displacements only. The top boundary was set to be fully free and the bottom layer was also assumed to be fully fixed.

Table 4.2: Boundary conditions of the unit cell, used in the numerical model.

Boundary Type	**Left**	**Right**	**Top**	**Bottom**
GW Flow	Closed	Open/Closed	Open	Open
Mechanical	Normally fixed	Normally fixed	Free	Fully fixed

4.3.2 Input

The parameter values used in the constitutive models are presented in this Section, displayed in Table 4.3. Parameters that are specific to certain material models are presented in subsequent sections. In Plaxis both the Mohr-Coulomb and Modified Cam Clay model can simulate increasing stiffness with depth, hence a uniform layer from -2 to -100 meters was created as the soil at Brf. Sydney has a uniform unit weight (γ) and friction angle (ϕ') from level -2. The permeability varies slightly over depth, therefore an average permeability calculated from the CRS-tests was chosen. Soil properties from undisturbed tests retrieved from the geotechnical investigations were used as input data. Furthermore, the initial void ratio e_{init}, was calculated using Equation 4.9 from Larsson (2008). The particle mass density of the soil ρ_s was assumed as 2.7 kg/m^3.

$$e = w\frac{\rho_s}{\rho_w} \tag{4.9}$$

Where w = Moisture content
ρ_s = Particle mass density of soil
ρ_w = Density of water

Table 4.3: General input parameters used in both constitutive models.

Parameter	Fill	Clay	Unit
Level	+2 to - 2	-2 to -100	m
γ_s/γ	20/18	16.5	kN/m^3
k	1.7E-9	1E-9	m/s
v	0.2	0.2	-
e_{init}	1.8	1.8	-
ϕ'	36	30	°

A rigid slab allowing for seepage was created, meaning that no water pressure is exerted onto the slab. The weight(w) was calculated using Equation 4.10, where the concrete was assumed to have a unit weight of 25 kN/m^3, and the thickness of the slab d_{real} to be equal to 0.5 meters. The anchors were made overly rigid to simulate a rigid and fixed slab, for the axisymmetrical model the out-of-plane center-to-center distance was chosen to be 1 radian. The Poisson's ratio was assumed to be 0.2.

$$w = (\gamma_{concrete} - \frac{1}{2}\gamma_{soil})d_{real} \tag{4.10}$$

4.3.2.1 Mohr-Coulomb model parameters

The specific parameters for the Mohr-Coulomb model are presented in Table 2.1. The oedometer modulus was calculated from the empirical formula presented in section 2.2.1 (i.e. $M = 500c_u$), as the oedometer modulus retrieved from the CRS test is considered too low. The increase in stiffness was calculated by assuming an average increase of shear strength throughout the soil depth.

Table 4.4: Input parameters in M-C model for the clay layer.

Mohr-Coulomb		
E'_{ref}	4500	$\mathrm{kN/m^2}$
G_{ref}	1875	$\mathrm{kN/m^2}$
E_{oed}	5000	$\mathrm{kN/m^2}$
E'_{inc}	648	$\mathrm{kN/m^2/m}$
ν'	0.2	-

4.3.2.2 MCC model parameter

The types of parameters used in this constitutive model are shown in Table 2.2. κ and λ for each layer were initially set to the values seen in 3.1, but were then calibrated through simulation of CRS tests. As previously presented the soil was also made uniform with a clay layer from -2 to -100 meter. The calibration was conducted with the goal of resembling the CRS tests found in the geotechnical investigation report. Furthermore, M_{CSL} was set to 1.4 to get a corresponding K_0^{nc} approximately of 0.6, due to the fact that the MCC-model is isotropic which could lead to an overestimation of the critical state line in extension. Table 4.5 encompasses all relevant input parameters for the clay layer, linked to the MCC model, used in the analysis.

Table 4.5: MCC stiffness parameters for the clay layer.

Modified Cam Clay	
λ	0.34
κ	0.034
OCR	1.3
M_{CSL}	1.4
ν'	0.2

4.3.3 Element level simulations

Element level simulations were performed for the MCC model, in which the swelling index κ and compression index λ were derived by comparing the generated graphs to the CRS lab data. In Figure 4.3, three different results can be observed, the measured data from the lab, and two soil test generated. One of the soil tests was generated with no initial effective stress, the other with an initial effective stress of -10 kPa in all directions. The inclination of the over-consolidated part of the curves closely resembles each other. However, the inclination of the virgin compression curve seems to be overestimated, when λ was set to be ten times as large as κ. Values for λ which corresponded to an inclination closer matching the CRS results were simulated, to study the impact this had on the simulated excess pore pressures induced by piling, but no significant impact was observed.

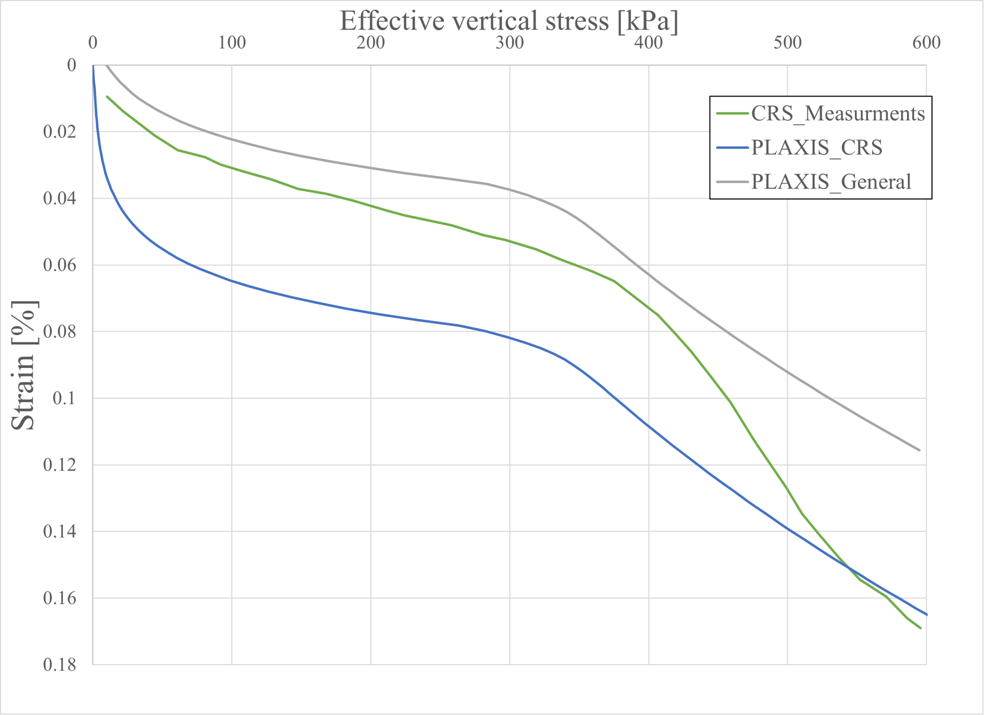

Figure 4.3: Comparison of calculated CRS-tests and measured

4.3.4 Oedeometer modulus

The stiffness for the different material models were plotted against depth to asses if the stiffness increases in a similar way. Using Equations 2.23, 4.11 and 4.4, an oedometer modulus corresponding to the value of the simulated compression index could be obtained and compared with the simulated response.

$$G = K' \frac{3(1-\nu')}{2(1+\nu')} \tag{4.11}$$

In Figure 4.4 the stiffness trends for the Mohr-Coulomb model (M-C), Modified Cam Clay model (MCC), and the empirical formula $E_{oed} = 500c_u$ are presented. For MCC this is the stiffness calculated for the initial effective stresses prior to construction. Also, derived values of M_0 from the CRS tests were multiplied with 3 and 5 and inserted. The CRS values were plotted to further confirm that the stiffness ratio used in the models is representative, as can be seen in Figure 4.4 all the trends are within the range $3 - 5M_{0,CRS}$.

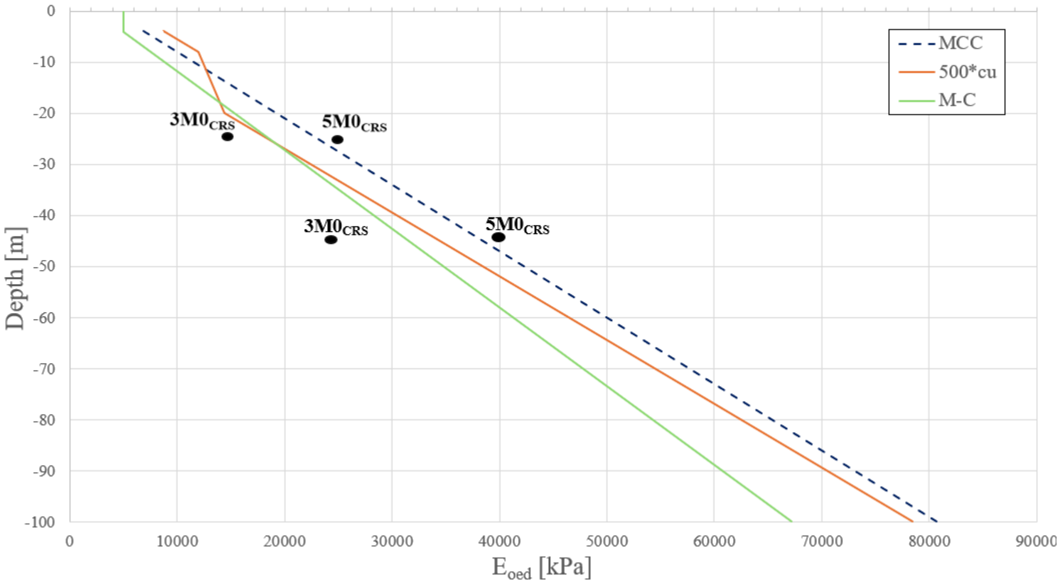

Figure 4.4: Increase of stiffness versus depth

4.3.5 Modelling of construction sequence

The excavation process at Brf. Sydney was delayed due to documentation of archaeological findings in the ground, which resulted in the piling being postponed. Also, contrary to Brf. Sydney, traditionally for safety reasons, piling is conducted from the ground level before the soil is excavated. Therefore two different order of construction scenarios were assessed in addition to a simple pile model:

1. **Simple pile model:** Only simulating pile installation.

2. **Case study:** The timeline of the center (C) excavation in Figure 3.3, was followed by the pile installation 182 days after completion of the excavation, see Figure 3.4.

3. **Reverse, case study:** The timeline of the center(C) in Figure 3.3 was reversed. The pile installation was placed first and thereafter, after 30 days a subsequent excavation was simulated.

Table 4.6 shows the phases used for scenario 1. In Table 4.7 the construction phases set in scenarios 2 and 3 can be observed. An initial phase with a "K0 procedure" was also calculated, thereafter all the phases were set to Consolidation (Staged construction) except the last one. The first excavation was in reality executed over 28 days, however, 10 days were applied in the model as the model does not represent the entire site, just the area shown in Figure 4.1. The displacements were reset to zero when the area was excavated down to level -1.8 m in both cases. The global groundwater table was assumed to be at level +0.5m, however, for the final excavation step, the groundwater table was set to the excavation bottom level, down to level -17 m.

Table 4.6: Construction phases for the simple pile model, scenario 1.

Pile model	
Pile installation	1 day
Consolidation	5 years

Table 4.7: Construction phases for scenarios 2 and 3 corresponding to Brf. Sydney and in reversed construction order.

Scenario 2: Case study		**Scenario 3: Reverse, case study**	
Excavation to +0.6m	10 days	Pile installation	1 day
Consolidation	150 days	Consolidation	30 days
Excavation to -2 m	51 days	Excavation to +0.6m	10 days
Consolidation	182 days	Consolidation	150 days
Pile installation	1 day	Excavation to -2 m	51 days
Consolidation	30 days	Consolidation ($t_{exc.toslab}$)	30 days
Slab installation	1 day	Slab installation	1 day
Consolidation	7 days	Consolidation	7 days
Consolidation	P-stop, 1 kN/m^2	Consolidation	P-stop, 1 kN/m^2

4.3.6 Parametric study

A parametric study was conducted to generalise the results and further study the impact on the effective heave pressure when varying the permeability and stiffness of the soil. The stiffness and permeability were chosen as they are two parameters that theoretically have large effects on the response of the soil, in terms of consolidation and dissipation. The parameters are both used when calculating the coefficient of consolidation(c_v), therefore also included in the formula for normalised time (T_v). Another reason as mentioned in section 2.2.1 is that the in-stitu stiffness can be difficult to determine as CRS tests usually underestimate the initial compression modulus. Different time steps between a finished excavation and installation of the slab were also used, as this is something that could vary from project to project. Graphs were created with generalised axes, normalised time T_v on the x-axis, and effective heave pressure ratio on the y-axis. In Table 4.8 the varied parameters can be seen, where the compression modulus M_0 corresponds to the average stiffness of the clay layer, and the permeability is assumed to be constant throughout the soil depth. A solution to Terzaghis one-dimensional consolidation theory proposed by Verruijt and Merwehoofd (1994) was used as a reference line in the graphs. Inspiration for the parametric study comes from Tornborg et al. (2024), especially for the design of the normalised graphs.

Table 4.8: Varied parameter values for the parametric study.

Parameters	**Varied values**
$t_{exc.toslab}$ [days]	1, 10, 30, 90, 365, 1825, 3650
k [m/s]	10^{-10}, 10^{-9}, 10^{-8}
M_0 [MPa]	36, 40, 50, 60

The parametric study was divided into two parts, the first part was conducted using the M-C parameters presented in Table 4.4, and the scenario 2 construction sequence shown in Table 4.7. The second part of the parametric study was conducted with a simplified construction order shown in Table 4.9, the stiffness (E_{oed}) of the soil was assumed constant, E'_{inc} was assumed to be 0. This was done to simulate the average stiffness of the soil, with no stiffness increase with depth. In both parts, first, only the excavation was simulated, and thereafter the pile installation was added. This was done to see what impact the pile installation had on the effective heave pressure.

Table 4.9: Scenario 4: Parametric study sequence

Scenario 4: Parametric study	
Pile installation	1 day
Excavation to -1.8 m	1 day
t$_{exc.toslab}$	see Table 4.8
Slab installation	1 day
Consolidation	P-stop, 1 kN/m^2

5

Result

This chapter presents the results obtained from the monitoring data and the analytical calculations. The computed results from the conducted numerical analyses are also presented, and in some parts compared to analytical results and the monitoring data.

5.1 Pore pressure data, Brf. Sydney.

In this section, the pore pressure data retrieved from the piezometers at Brf. Sydney will be presented. The data for the excavation and piling will be presented separately and then compared to each other.

5.1.1 Pore pressure during excavation

In Figure 5.1 the excess pore pressure during the excavation is presented, along with the excavation timeline where the colored horizontal lines correspond to the zones in Figure 3.3 and dates. The installation dates of the piezometers are presented in Table 5.1, and the first excavation stage started March 3rd 2024. As shown in Figure 5.1, the monitoring data at all depths indicates that a stationary pore pressure level had not been reached at the start of the excavation process. It is therefore difficult to observe if there was a decrease in pore pressure from the static level, during excavation. However, one observation is that during the excavation of the center zone, the pore pressure drops at a depth of 5m, generating negative excess pore pressure at the surface. One deviation seen in Figure 5.1 is the increase and decrease of pore pressure between May and September, attributed to the data for depth 20m, this trend cannot be seen at any other depth. Another deviation, attributed to the data from 40 m depth, is the almost linear increase occurring from October and forward.

Table 5.1: Dates of installation of piezometers.

Piezometer	**Installation dates**
5m	23/2 - 2023
10m	23/2 - 2023
15m	23/2 - 2023
20m	24/2 - 2023
40m	28/2 - 2023

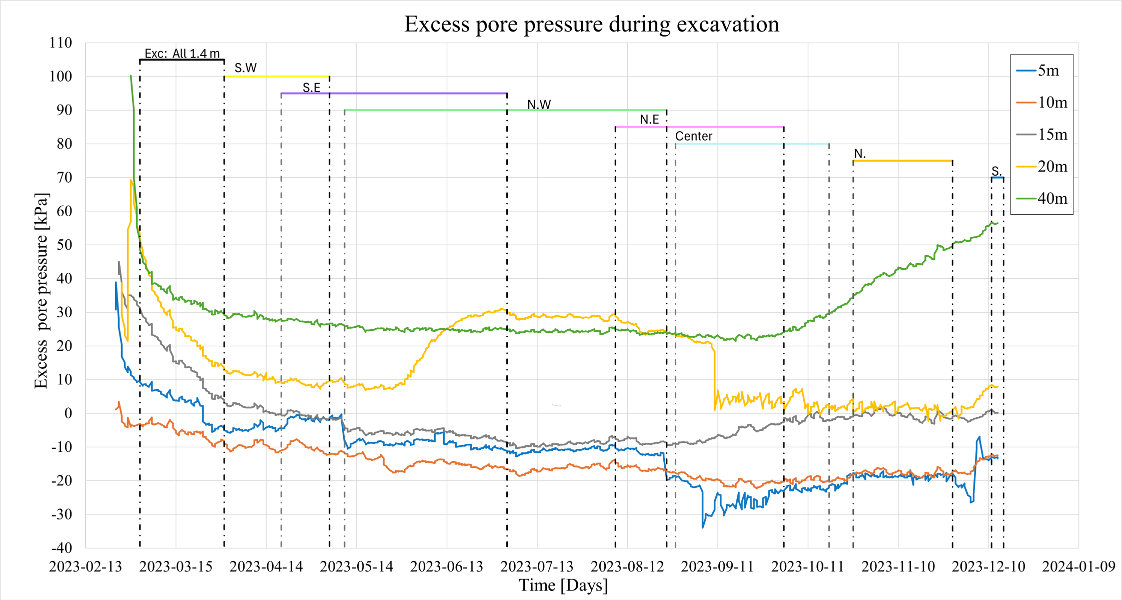

Figure 5.1: Excess pore pressure development during excavation, field monitoring data. See Figure 3.3 for the location of excavation areas within the site.

5.1.2 Analytical calculation of excess pore pressure due to excavation

The results from the analytical calculation of the excess pore pressures generated by unloading are shown in Figure 5.2. There are some factors that the analytical calculations do not account for, mainly the effect of the surroundings of Brf. Sydney and the time-dependent consolidation of the pore pressures. The analytical results rather show the potential negative excess pore pressure each excavation phase generates at the different depths studied. Although the differences between the analytical results and the measurements are large (mainly due to stationary pore pressure not reached after installation of the piezometers), a few similarities are worth mentioning. The negative excess pore pressure decreases with depth, this appears to be largely consistent between the analytical results and the measurements. Additionally, during the excavation of the center part, both the analytical results and the monitoring data show a decrease in pore pressure, however, the analytical result shows a larger difference. To summarise, the trends show similar decreases during excavation, but due to the excavation occurring in stages, large differences in pore pressure are not noticeable.

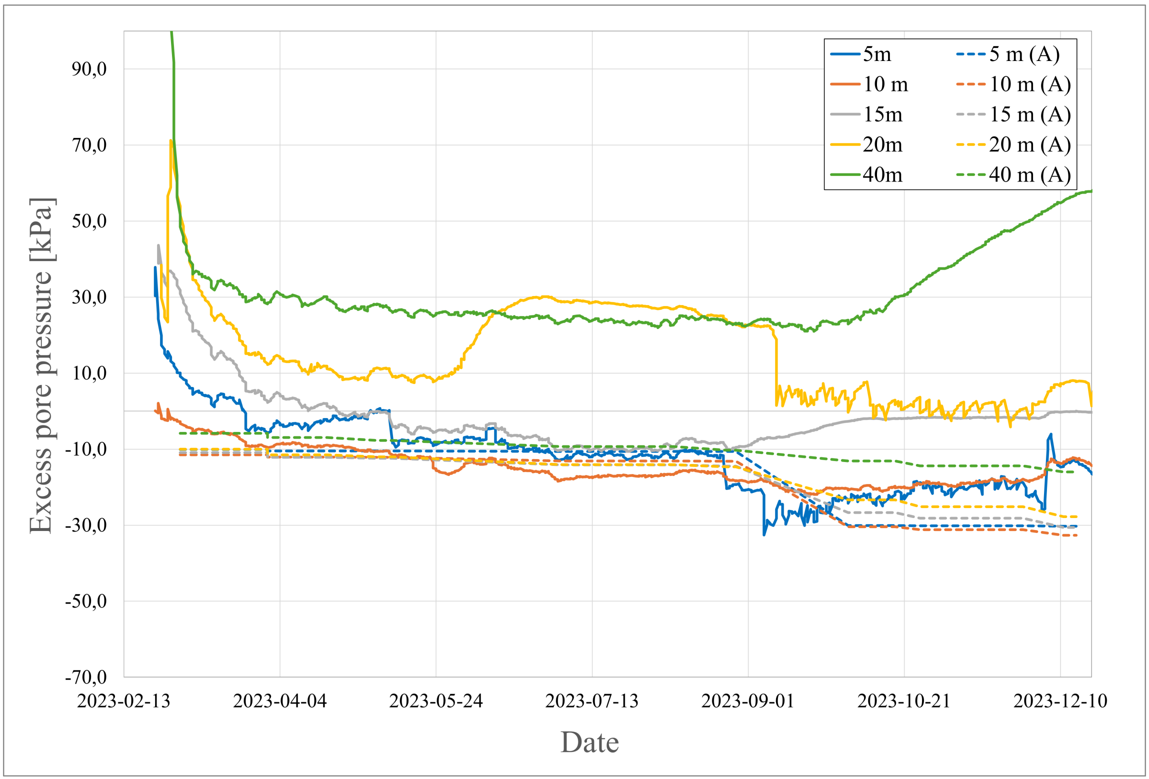

Figure 5.2: Analytical calculations of excess pore pressure results, compared to monitoring data. (A) denotes analytically calculated excess pore pressures (see section 4.2).

5.1.3 Pore pressure during piling

The excess pore pressure measured during piling is shown in Figure 5.3. The effects of pile driving are noticeable in the plot, especially in the spikes presented at certain depths and times in the data. The first major spike appeared on 29/1 - 2024, which is when the piles located just left of the piezometers, as seen in Figure 5.4, was installed. The second, slightly larger spike appears at the same time (27/2 - 2024) as the installation of the piles located in the center of the simulated unit cell. None of the piezometers are in such proximity to a pile that they will experience the pore pressures associated with the plastic zone, therefore none of the high excess pore pressures seen in the analytical calculations (see section 5.2) can be observed in the measured data. Furthermore, due to the pre-augering of the first 15 m of the piles, no spikes or peaks are observed in the data from the piezometers located at 5, 10, and 15-meter depths.

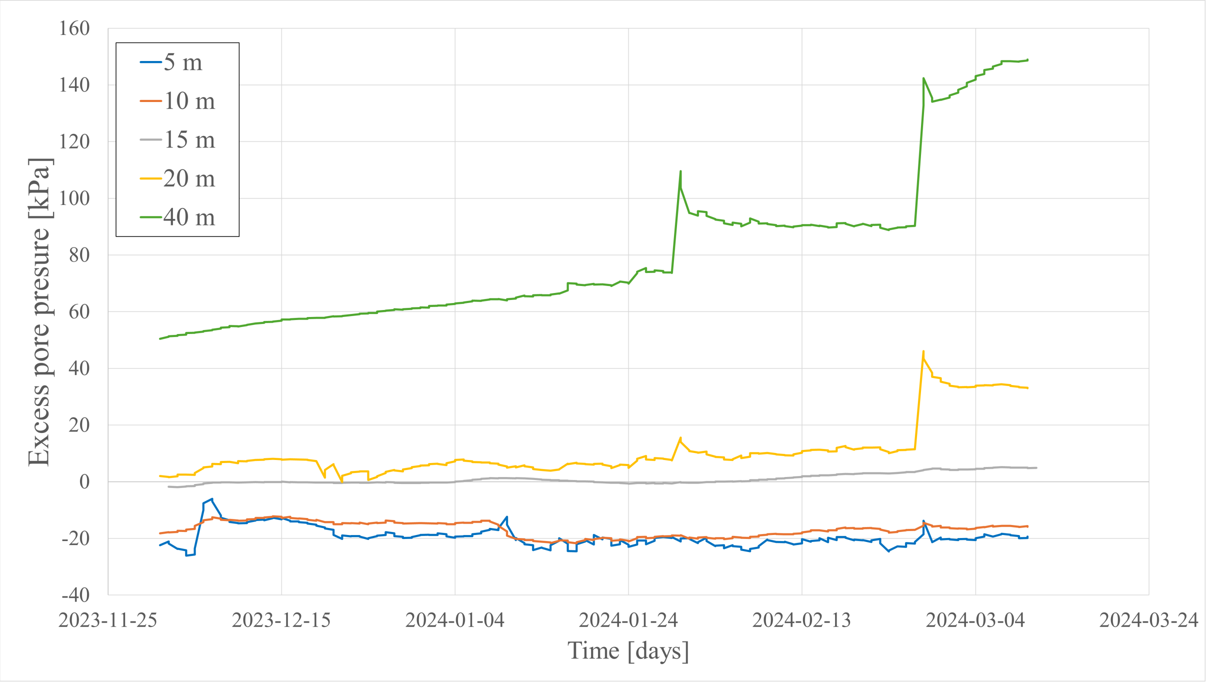

Figure 5.3: Excess pore pressure development during pile installation, data from Brf. Sydney.

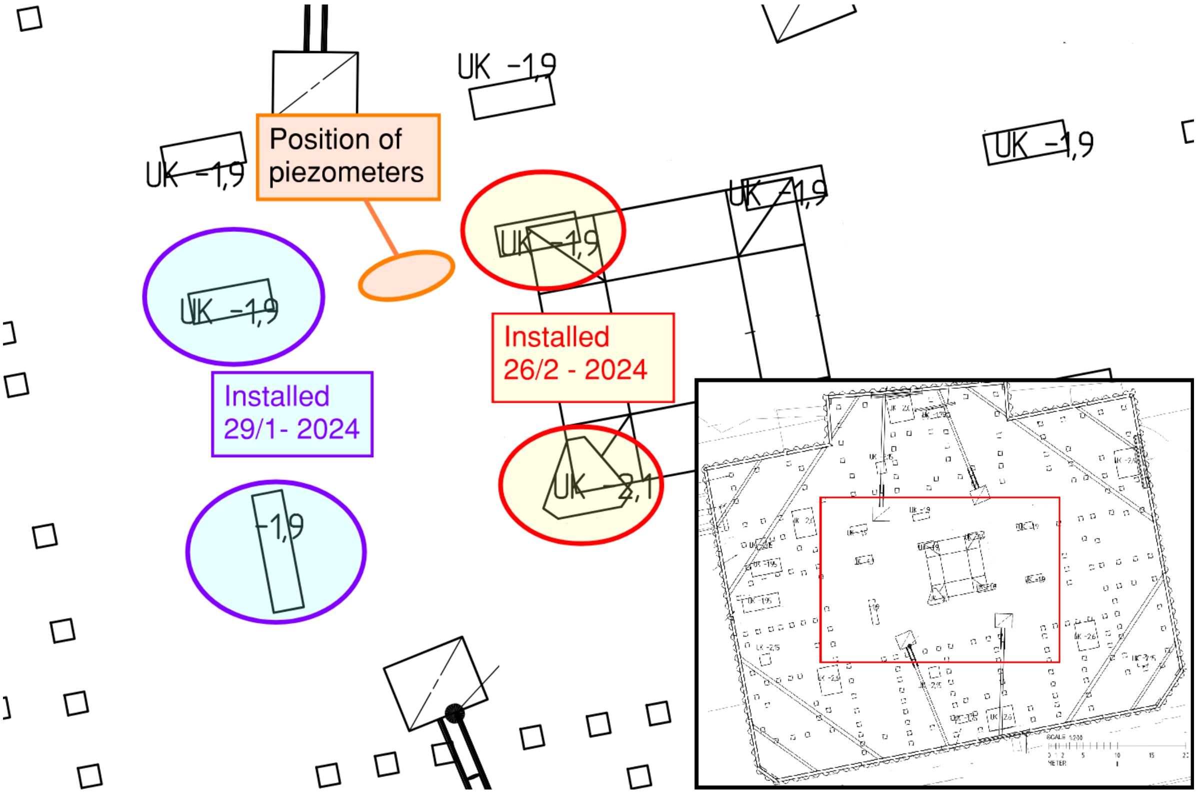

Figure 5.4: Installation dates of piles in close proximity to the piezometers.

5.2 Piling response

In this part the results from the simple pile model generated in Plaxis 2D (version 2022.01) is compared to analytical results obtained through the method of Randolph and Wroth (1979). These include both excess pore pressures due to pile driving, and time dependent consolidation. The piling response in the numerical analysis has been simulated using both Mohr-Coulomb and Modified Cam Clay constitutive models, both of which will be shown in the results. In summary, it can be observed, that the response generated by the simple pile model, is largely consistent with theory regarding excess pore pressure caused by piling and subsequent dissipation. The choice of constitutive model mainly impacts the magnitude of the initial excess pore pressures, when comparing results gathered by the constitutive models. This might be a result of the stress path reaching the critical state line in the MCC model, which has the possibility to generate large shear stresses (see section 2.7.3.4).

5.2.1 Plastic zone

The plastic zone was analytically calculated using Equation 4.3, which resulted in $r_{pl} = 2.87$ m. Examining the plastic points generated in the Mohr-Coulomb model in the numerical model during the pile installation phase, shows that the model generates a similar plastic zone as compared to the analytical method. All nodes spanning from the left boundary to a radial distance of 2.6 m are classed as "failure points" indicating that the M-C model generates a plastic zone equivalent to $r_{pl} = 2.6$ m.
Examining the same type of output for the MCC model shows a zone of "cap points", that spans from the left boundary to a radial distance of 2.25 m. This means that the MCC model generates a zone of where the stress state have reached the yield surface.

5.2.2 Initial excess pore pressure distribution

Figure 5.5 displays the initial radial variation of the excess pore pressure at different depths. From these results, there is a clear indication that initial excess pore pressures increases with depth across all analyses, which is logical considering that the undrained shear strength c_u increases with depth. Due to the constant stiffness ratio G/c_u with depth, the plastic zone generated by Randolph's method (1979) is equal throughout the depth. The numerical results generated by the Mohr-Coulomb model, portrayed by the dashed lines, shows a response similar to the analytical results. It is noteworthy that at 18 m depth, the excess pore pressure is overestimated compared to the analytical results, whereas it's slightly underestimated at larger depths. But, overall they roughly generate a similar response, especially with increasing radial distance from the pile face. The pore pressures generated by the Modified Cam Clay model deviates greatly from the other results, particularly at the pile face. This seems to be a fallout of using this model. However, at approximately 2 meter from pile face the difference in pore pressure between the models start to diminish.

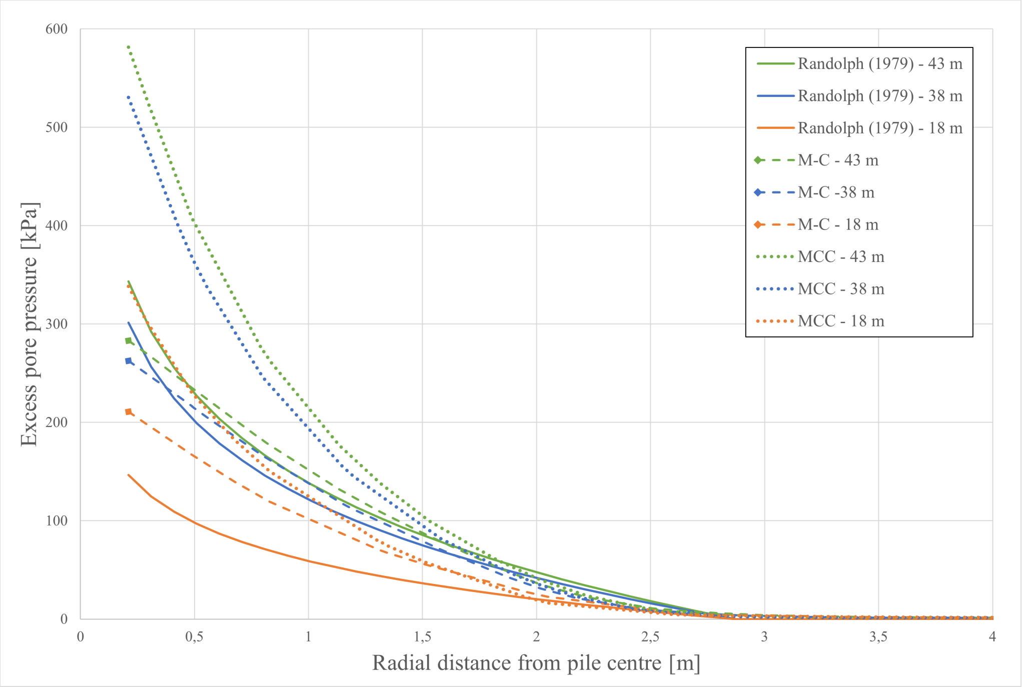

Figure 5.5: Calculated initial radial variation of excess pore pressures.

5.2.3 Pore pressure variation at pile face with time

Figure 5.6 shows how the excess pore pressure at the pile face varies with time, at different depths. One thing that needs to be considered for these results, is that the time in the numerical analysis starts from 1 day, whereas the analytical results start from 0 days. To adjust for this, 1 day has been added to the analytical results, making them easier to plot alongside the numerical results. The analytical results also have significantly higher resolution of results at the start of the analysis, particularly within the first 10 days. The analytically calculated excess pore pressures dissipate rapidly during the first 10 days, while the numerical dissipation is more gradual. Within 10 - 100 days, the differences between the different results clearly diminish. The time-dependent response at the pile face of both the numerical material models is comparable to the analytical response, especially when analysing larger time frames (i.e. $t > 10$ days).

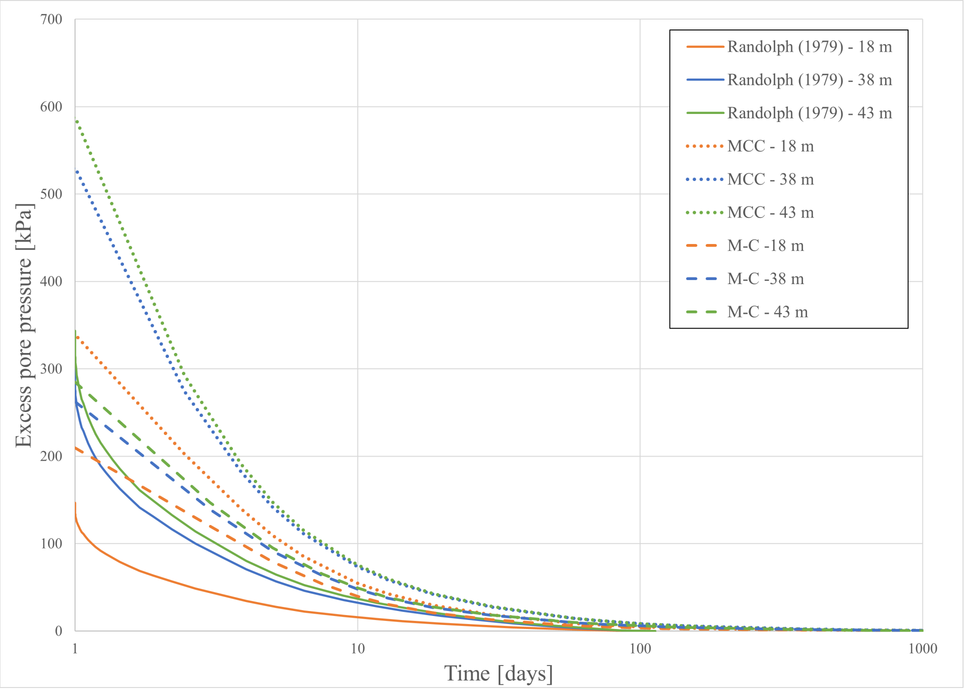

Figure 5.6: Variation of excess pore pressures at pile face with time, for different depths.

5.2.4 Variation of radial excess pore pressure distribution with time.

Figure 5.7 and 5.8 displays the variation of radial excess pore pressures with time, for the two material models used in the numerical analysis. The axes have been normalised in the plots, to make the results more comparable to the graphs found in Randolph and Wroth (1979) and Randolph (2003). The values of time in days, corresponding to each time factor T, are displayed in Table 5.2. As previously mentioned, the stiffness ratio that applies for the soil conditions at Brf. Sydney, also modelled in the numerical model, is $G/c_u = 187.5$, which is larger than the stiffness ratio of the soil conditions seen in Randolphs results ($G/c_u = 187.5$ in Randolph and Wroth, 1979, $G/c_u = 100$ in Randolph, 2003). The results show that both M-C and MCC mobilise a similar normalised timed response as the theoretical response seen in Figures 2.3 and 2.4. As seen in Figure 2.2, a larger stiffness ratio is associated with larger excess pore pressures at all time factors. This correlation can be observed in the result from the numerical model, where similar time factors correspond to larger pore pressures. The large pressures generated by the Modified Cam Clay model (compared to M-C) are noticeable in these results as well. These larger pressures dissipate quicker than the Mohr-Coulomb model, leading to a mostly similar response over time.

Table 5.2: Time (in days) corresponding to the time factors displayed in the results.

Time factor T	**Time in days**
0	0
6	1
22	4
50	9
274	49

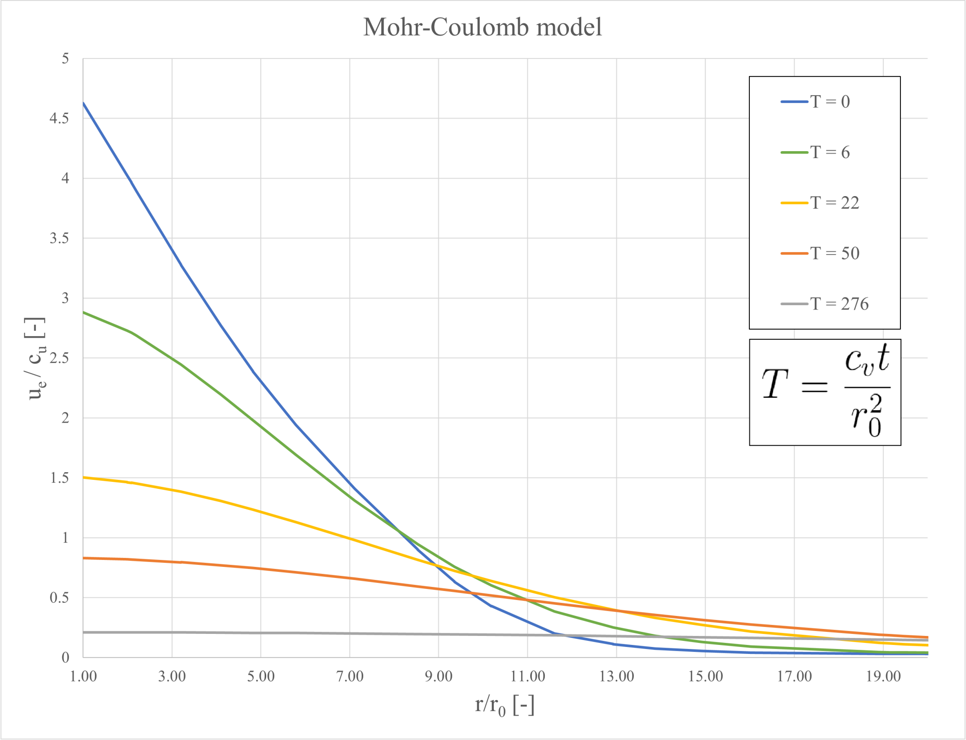

Figure 5.7: Variation of excess pore pressures with time, using Mohr-Coulomb material model

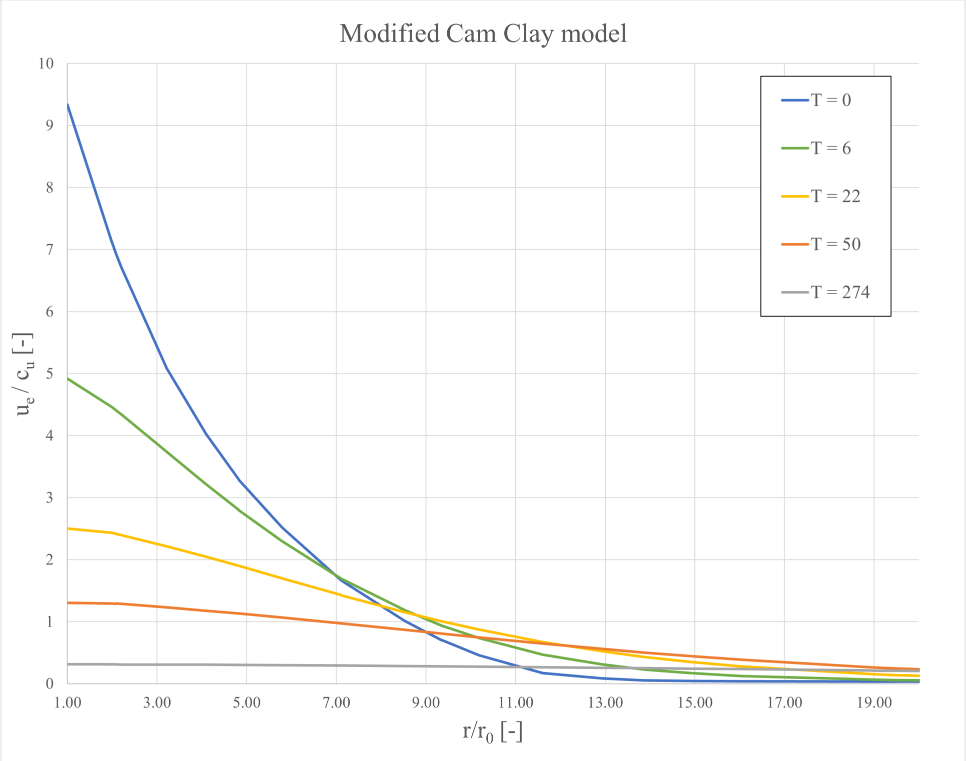

Figure 5.8: Variation of excess pore pressures with time, using Modified Cam clay material model.

5.3 Excavation and pile installation in combination, with a construction time corresponding to Brf. Sydney

In this section the computed pore pressure during construction (excavating and piling) of the foundation, as well as the effective heave pressure and displacements under the slab are presented. The analyses were conducted using the unit cell presented in subsection 4.3.1. Comparisons are made between the two constitutive models used for the numerical analysis, the different sequences of construction, and the monitored pore pressure data. One thing to bear in mind is that all the excavation stages were not included in the numerical model, only the excavation done at the center zone, as this is where the piezometers are placed. Also, only one of the nearby pile installations is simulated in the numerical model.

5.3.1 Effective heave pressure, with a construction time corresponding to Brf. Sydney

In Figure 5.9 the effective heave pressure EHP at the center of the slab in the unit cell, versus normalised time is presented. The effective vertical stress $\sigma'_{n,center}$ was computed with the numerical model using the constitutive model Mohr-Coulomb, the highest generated stress on the slab until fully consolidated was used. As explained in subsection 4.3.2 there is no water pressure on the slab (this is an idealisation used in this study), hence the EHP is normalised against σ'_0. The reverse construction sequence of Brf. Sydney was used (see scenario 3 in Table 4.7) when computing the effective vertical stress. The blue markers in the figure represent the EHP generated when the construction only consists of excavation/unloading (scenario 3, without the pile installation), the graph shows that the consolidation response of the unloading model is similar to the one-dimensional consolidation theory by Terzaghi. However, the model only generated a heave pressure equal to 80% of the relieved load. The grey markers represent the reversed case (see Table 4.7), i.e. first pile driving, thereafter excavating. For the reversed case (Pile+Unloading) the heave pressure decreases with 20-25% compared to the case of only unloading. However, for larger values of T_v both cases converge towards the Terzhagi consolidation line.

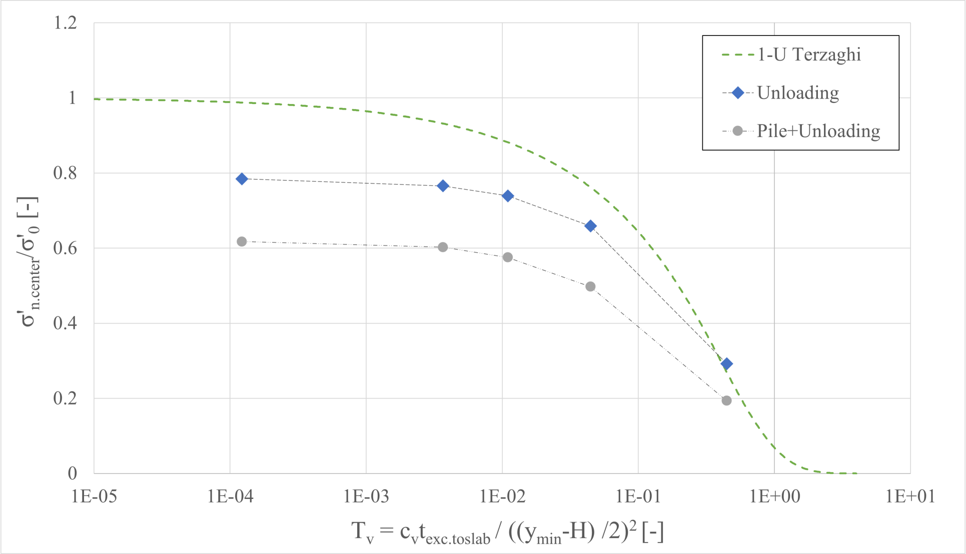

Figure 5.9: Normalised effective heave pressure at center of slab, versus normalised time (inspired by Tornborg et al., 2024)

5.3.2 Excess pore pressure evolution, with a construction time corresponding to Brf. Sydney

Figure 5.10 shows how the computed excess pore pressures varies at different depths, 3 meters from the pile (which is based on the distance between piezometers and nearest pile), with time when considering the case study time schedule, i.e. excavation followed by piling. The first excavation phase takes 10 days (see subsection 4.3.5, where the maximum negative excess pore pressure reached is approximately -25 kPa uniformly over the clay deposit, due to the unit cell geometry considered in this analysis. Afterward, a consolidation period over 150 days occurs. As the left and right boundaries are closed the model only dissipates excess pore pressure upwards and downwards. Therefore, the soil closest to the surface consolidates faster than the soil in the middle of the deposit, as can be observed in Figure 5.10. The next excavation simulated over 51 days generates the highest excess pore pressure in the middle of the clay deposit. The following consolidation period (182 days) shows a similarity to the first consolidation period, in that the soil layers closest to the surface consolidates faster. The pile installation causes a reduction of the negative excess pore pressure at the elevations -18 m and -38 m, whereas, the pore pressure is unaffected in the top soil layer, since a pre-augering of down to -15 m is simulated. After the pile installation the top layers continues to consolidate, while the lower levels experience an initial decrease, followed by an increase in negative excess pore pressure observed at elevations -18 and -38 m until the slab is cast. When the slab is cast it takes slightly more than 19 years for the excess pore pressures to consolidate completely.

Figure 5.10 also displays results for both constitutive models used in the numerical analysis. The largest negative excess pore pressure is reached after the second excavation phase for all simulated elevations and both material models. Mohr-Coulomb (M-C) and Modified Cam Clay (MCC) broadly produce similar results up until the slab is installed, after which the models starts to differ in the results. M-C generates a small but instant reduction in negative excess pore pressures as a response to the installation of the slab. Conversely, MCC generates an increase of negative excess pore pressures, but this response is not as instant as the increase observed in the M-C results. This response levels of after approximately 50 days after which the excess pore pressures starts to increase similarly to M-C. Overall the models produces similar results and after 1000 days the differences between the models starts to diminish. Henceforth, the reverse construction order analysis was done using Mohr-Coulomb exclusively, for simplicity and efficiency with regards to computing the results.

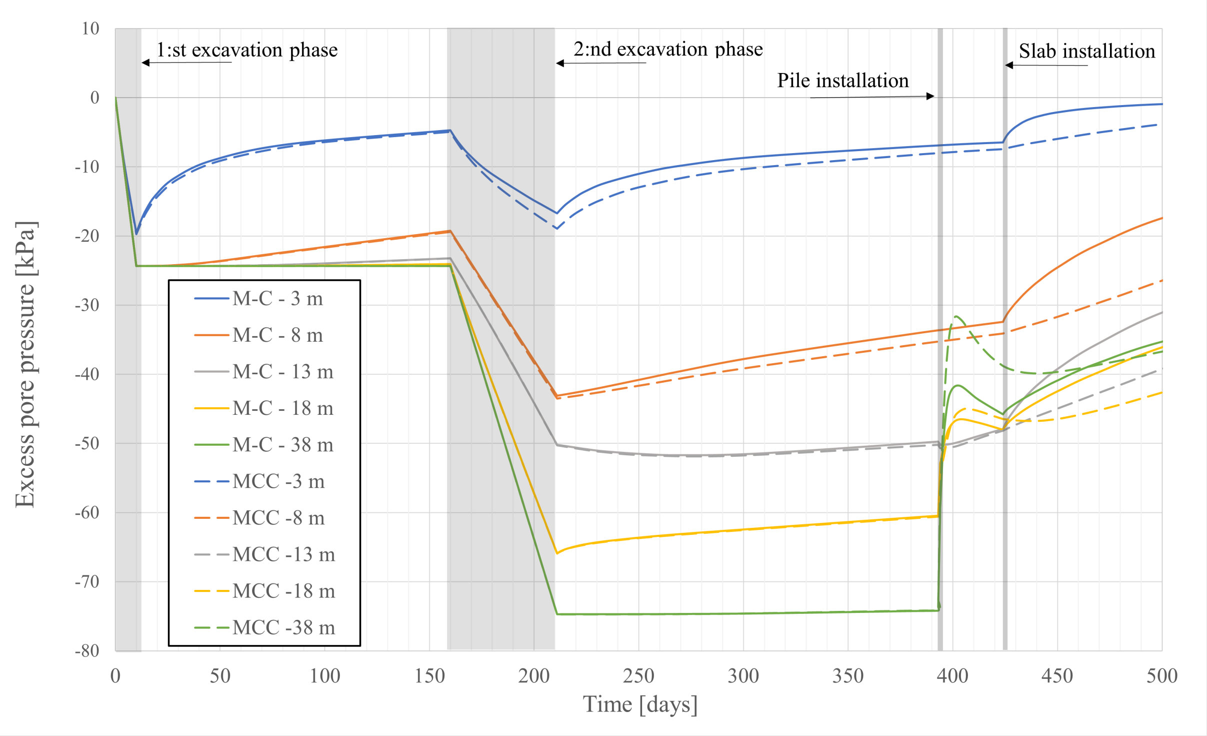

Figure a)

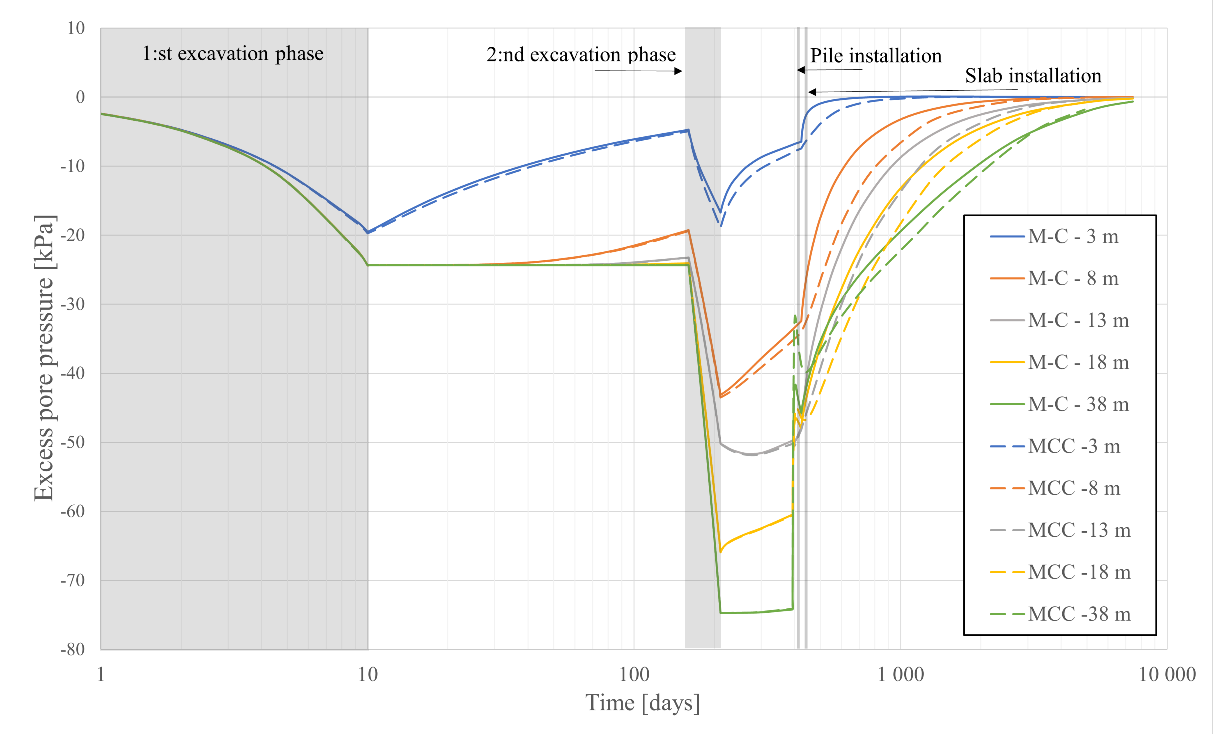

Figure b)

Figure 5.10: Variation of computed excess pore pressures at 3 meters from the pile, construction order corresponding to Brf. Sydney, see table 4.7, i.e. excavation before piling. a) Linear time axis. b) Logarithmic time axis.

5.3.3 Excess pore pressure evolution, with a reversed construction sequence

Figure 5.11 displays how the excess pore pressure varies at different depths, when piling is simulated prior to excavation using the Mohr-Coulomb model. What sets these results apart is that the original case (excavation before piling) generates greater negative excess pore pressures than the reversed case. Additionally, the excess pore pressures during the first phases of the calculations are positive as a result of the pile installation, with these pressures then being lowered to negative excess pore pressures during the excavation phases although of lower magnitude than in the previous analysis. The largest negative excess pore pressure is generated at -18 m depth in this analysis, as opposed to -38 m in the prior analysis with the actual construction sequence. Furthermore, the pore pressure evolution at -3 m differs from the other simulated depths between the excavation phases. At -3 m the excess pore pressures generated by the pile installation, dissipate quicker than the other levels. This is likely due to -3 m being far enough from the pile installation, and its close proximity to the surface (which has a draining effect), which causes these pore pressures to consolidate quickly. This can be seen in Figure 5.12, which shows the excess pore pressure evolution in the numerical model during stages 1-4. The numerical model is fully consolidated just after 7500 days.

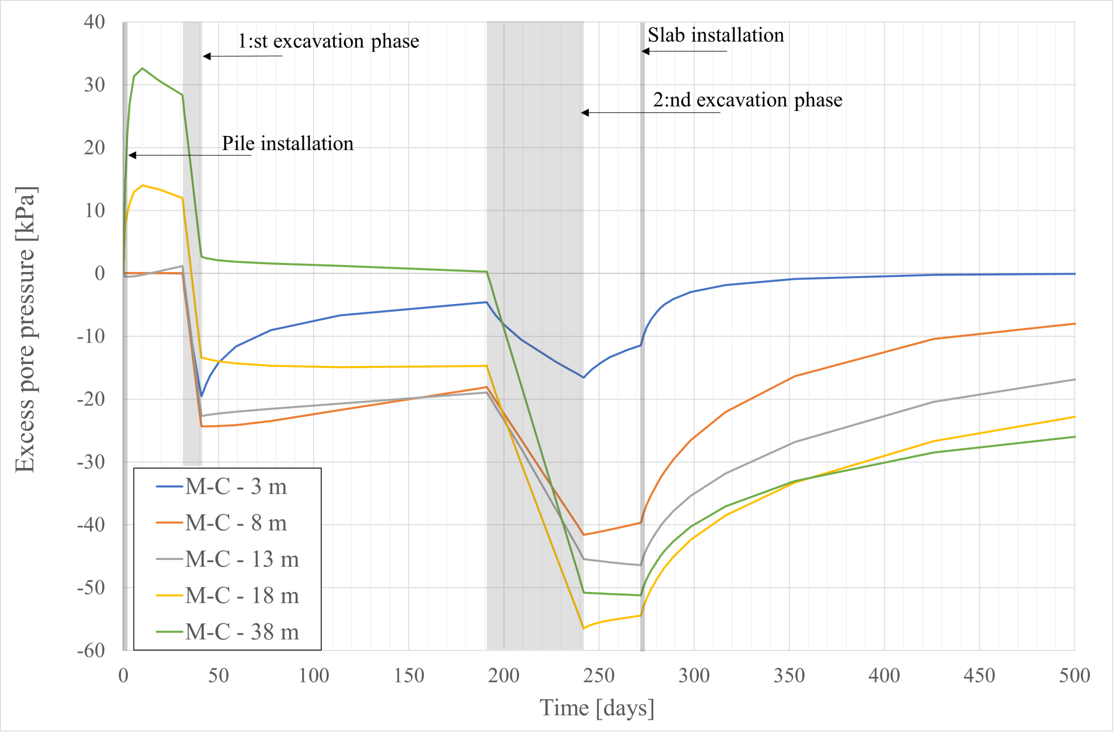

Figure a)

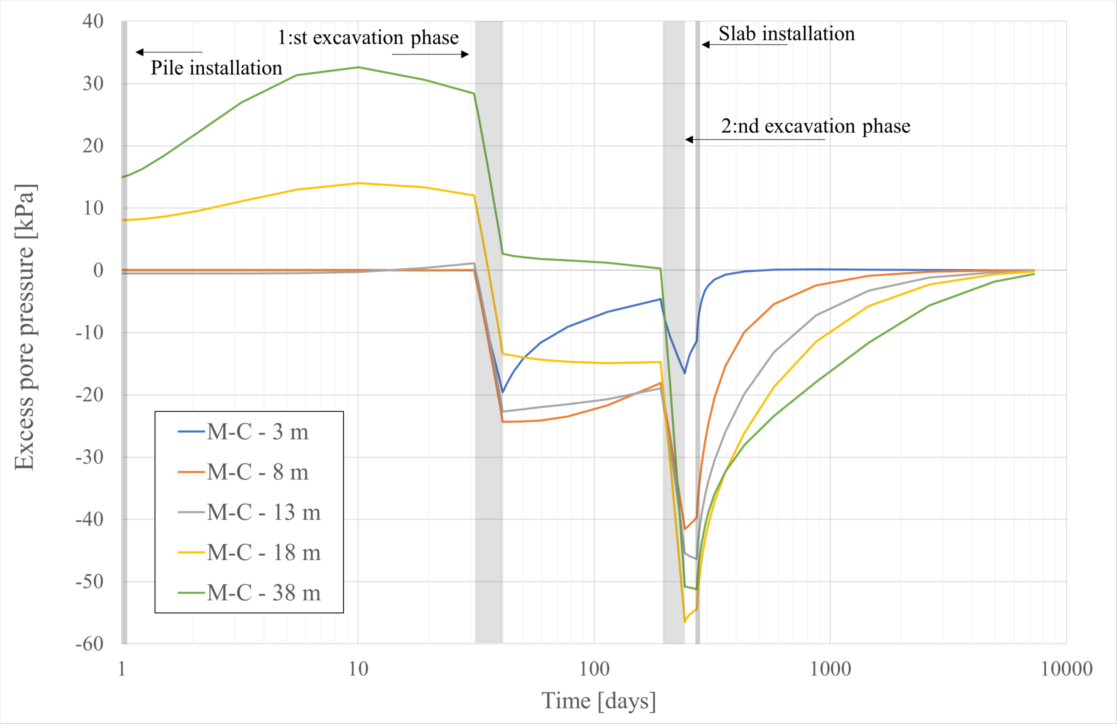

Figure b)

Figure 5.11: Variation of computed excess pore pressures at 3 meters from the pile, with the reverse construction order, i.e. piling before excavation. a) Linear time axis. b) Logarithmic time axis.

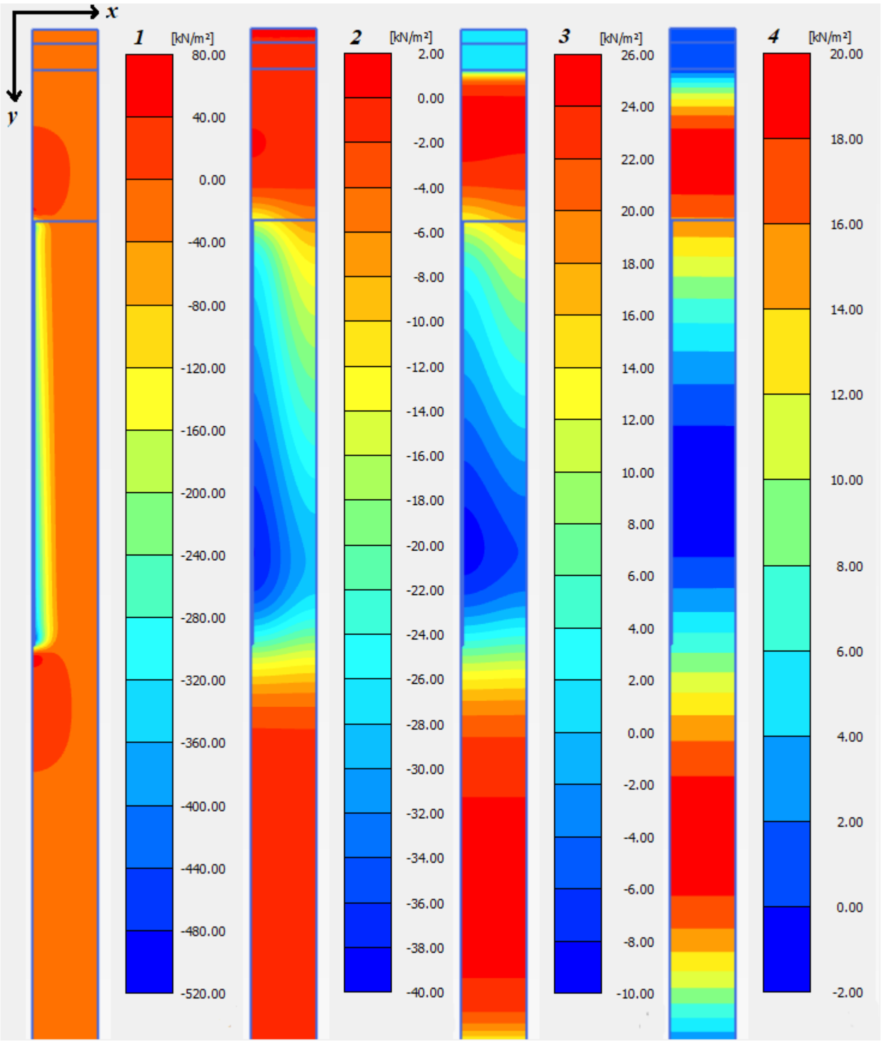

Figure 5.12: Excess pore pressures throughout the model, during stages 1 to 4, for the reversed construction order (See Table 4.7). In Plaxis the sign convention is reversed, thus negative values correspond to positive excess pore pressures.

5.3.4 Vertical displacement beneath the slab.

Figure 5.13 shows the vertical displacement 1 meter below the excavation bottom over time. The generated displacement when using the same sequence of construction as Brf. sydney (unloading→ Pile installation), using M-C and MCC is shown in Figure 5.13. The vertical displacements for the reverse construction order using M-C is displayed in Figure 5.14. The original sequence was simulated with both the constitutive models, the reversed order was only calculated using M-C. Observed in the Figure 5.13 and Figure 5.14, the original sequence generates the largest displacement. Of the two material models (M-C and MCC) MCC gives the largest deformation. The computed deformation of the reversed construction sequence is significantly lower than the order used at Brf. Sydney.

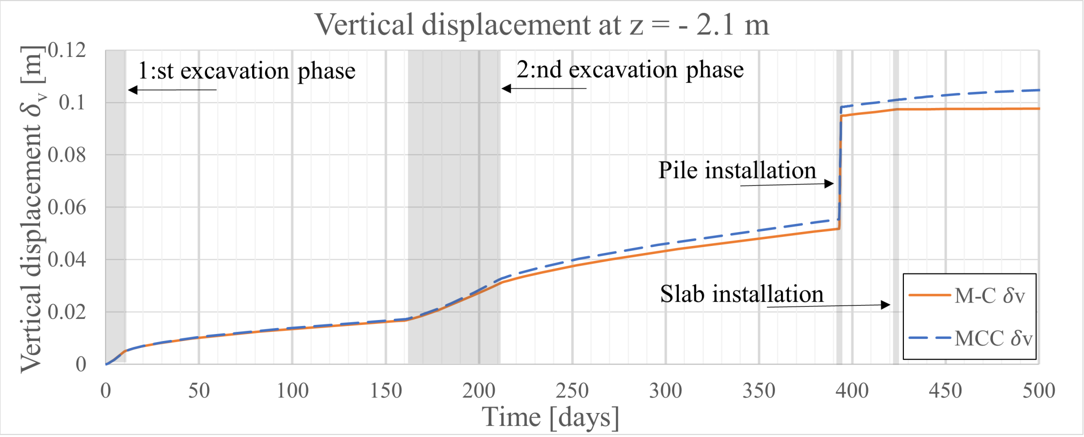

Figure 5.13: Vertical displacement below the excavation bottom for the Brf. Sydney case, see Table 4.7.

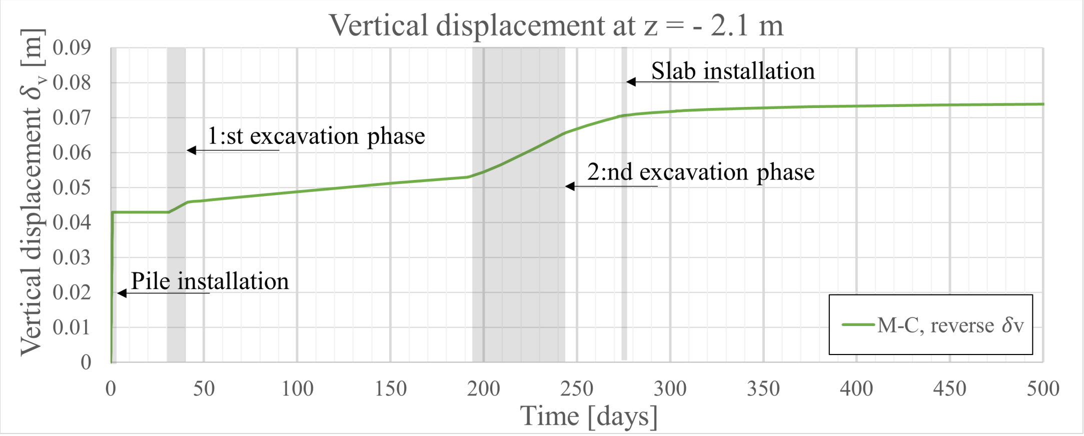

Figure 5.14: Vertical displacement below the excavation bottom for the reversed case, see Table 4.7.

5.3.5 Comparison of computed, and measured values for the pore pressure

In Figure 5.15 the measured pore pressure from Brf. Sydney and the computed pore pressure from the numerical model is presented. As mentioned in the introduction (Section 5.3) of this section, one thing to bear in mind is that all the excavation stages were not included in the numerical model and that only one of the nearby pile installations is simulated. It can be observed that the measured and computed pore pressure at level -3 meters share similarities, a small decrease in pore pressure from the first excavation and then a more immediate decrease for the center excavation. The measured trend for level -3 meter fluctuates considerably, which may be due to the fact that it is only 1 meter below the excavation bottom, heavy construction equipment driving over the piezometers could affect the result. The trends for level -8 meters share similarities, but the excavation of the center zone does not seem to have a significant impact on the measured pore pressure contrary to the computed.

At level -13 meters the trend differs considerably, the trend does not start at the same static pore pressure, however, the decrease in pore pressure from the first excavation is comparable. As the measured trend at level -8 meters, the trend at level -13 meters is not affected by the excavation at the center zone. The trend at level -18 meters starts with a decrease similar to the computed pore pressure, but not at the same static level. The measured trend also has an inexplicable rise in pore pressure in June, 2023, which stabilises, and then returns to what probably is its static pore pressure level in late August. The measured trend at level -18 meters does not react to the excavation of the center zone, however, it has a pore pressure increase when the pile is installed in February 2024. At level -38 meter the measured pore pressure does not seem to reach its static pore pressure, in October something happens with the piezometer, and the pore pressure increases linearly. The only thing that could be used for comparison to the computed pore pressure is the increase of pore pressure at the time of pile installation. The computed pore pressure at levels -18 and -38m do not have a noticeable consolidation between the excavation phases, due to the thickness of the layer.

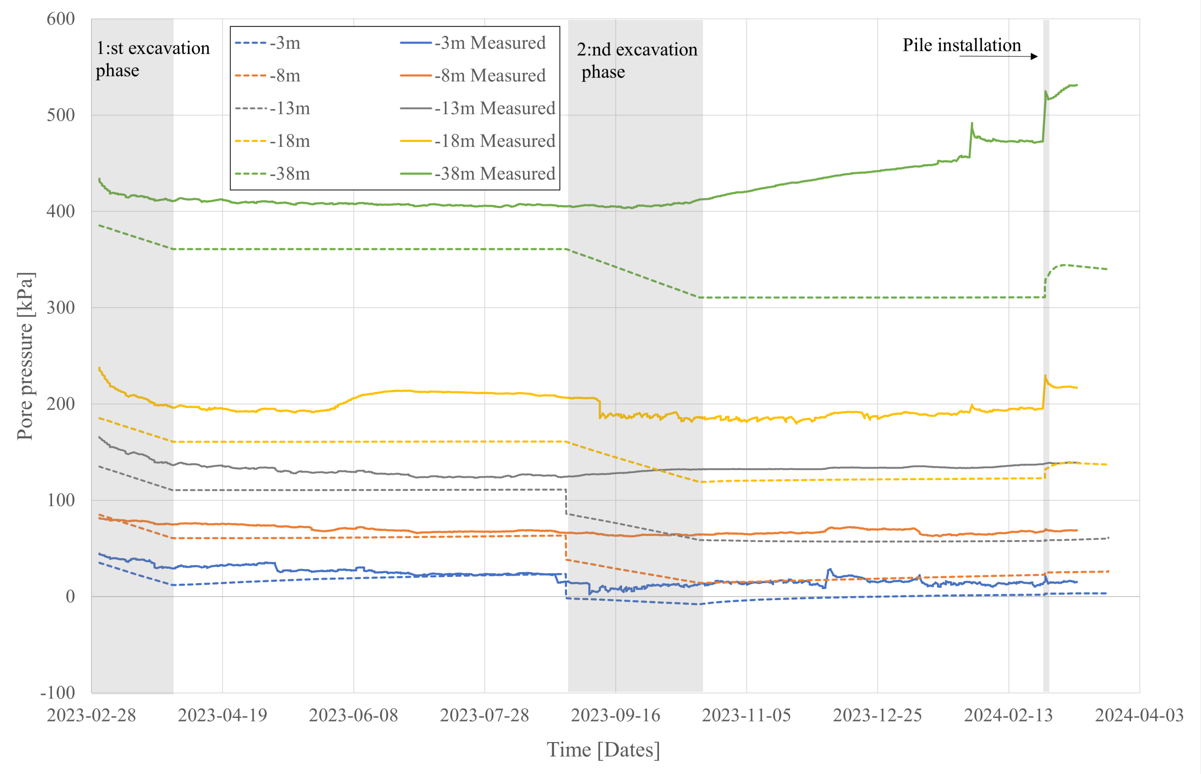

Figure 5.15: Pore pressure over time, measured at Brf. Sydney and computed from the numerical model

5.3.6 Parametric study

A parametric study using the M-C model was conducted to see how the permeability (hydraulic conductivity) and stiffness of the soil impact the effective heave pressure (EHP). The parametric study considers two cases, one with only unloading and one with piling followed by unloading. The varied parameters can be seen in Table 4.8. The time from excavation completion to slab activation, ($t_{exc.toslab}$) was used for all permeabilities. The results can be compared to Figure 5.9 where a permeability specific for conditions at Brf. Sydney was used.

In Figure 5.16 the impact of varying the average permeability (see subsection 4.3.6) of the soil is presented. In the figure it can be observed that the permeability has a large influence on the consolidation time. A lower permeability gives a longer consolidation time, whereas a higher permeability gives a shorter consolidation time. The red markers represent the lower permeability, and as they have not approached zero it means that the soil has not consolidated completely, even after the largest simulated $t_{exc.toslab}$, a high EHP is still present on the slab.
Similar to Figure 5.9 the pile installation reduces the heave pressure generated on the fixed slab. Observed in Figure 5.16 the heave pressure on the slab is reduced by 20% when simulating both the pile installation and the excavation.

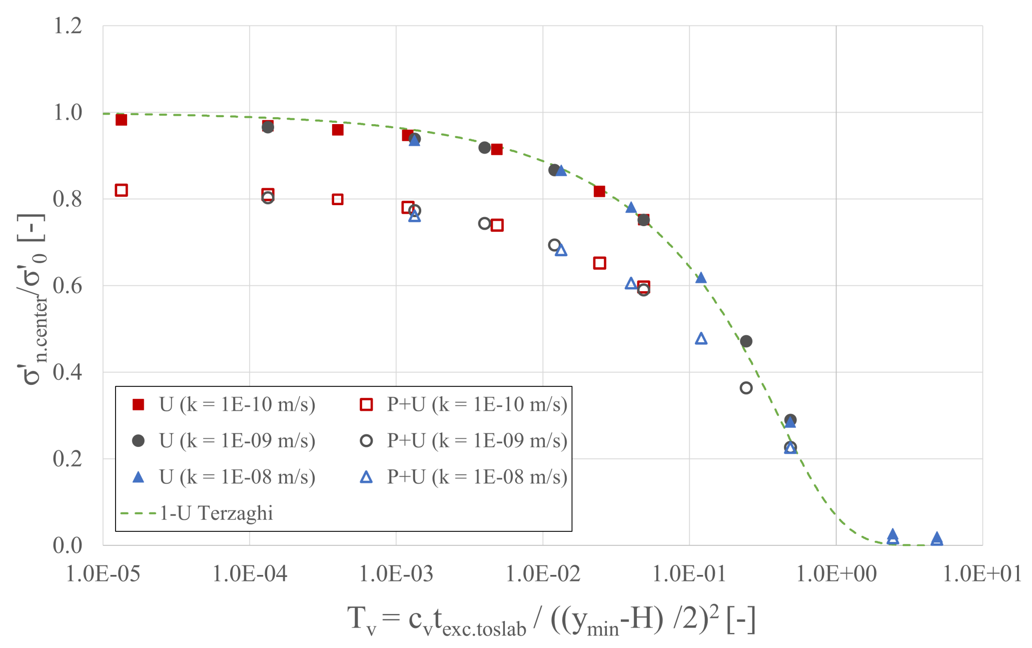

Figure 5.16: Impact of permeability on EHP (P+U denoted piling before excavation)

Figure 5.17 shows the impact on effective heave pressure that an increase in stiffness has. It can be observed when adding the pile installation (P+U), that a larger soil stiffness is associated with a decrease in EHP. When only unloading the soil (U), no such behavior is observed. Increasing stiffness for the case of unloading, only equates to a shorter consolidation time.

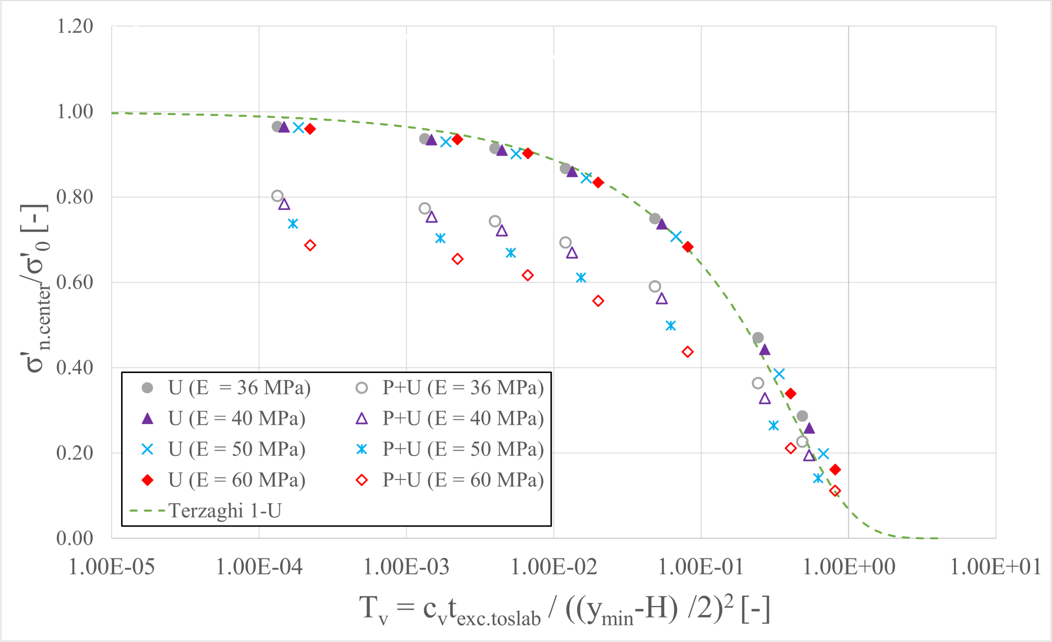

Figure 5.17: Impact of stiffness on EHP (P+U denotes piling+excavation)

6

Discussion

In this chapter the results and methodology will be discussed.

6.1 Measured pore pressure data

The construction of the foundation of Brf. Sydney was less than ideal, primarily being slowed and prolonged by the required preservation and documentation of the archaeology in the ground. The archeology also was the reason for the unconventional (in Gothenburg) construction sequence of excavating before piling. Another outcome was that the excavation was open and exposed for a longer period allowing for negative excess pore pressures to dissipate more than in a typical project. This outcome brought difficulties in trying to assess whether the piling could counteract the excavation in terms of excess pore pressures. If the excavation could have been more efficient, mainly by having a much shorter time between excavating and piling, perhaps the counteracting effect between the unloading and piling would have been more substantial. As was the case, the negative excess pore pressures were allowed to dissipate for 332 days (combined for the two excavation phases) before piling was commenced, which means that part of the negative excess pore pressure that could have been reduced by piling, had already dissipated. In addition, the second excavation phase goes on for quite a long time when compared to the first, 51 days as opposed to 10 days respectively. Further studies including field monitoring targeting this particular topic could do a more comprehensive analysis of the counteraction with regard to excess pore pressures, caused by excavating and piling activities.

The deviations and overall irregularity present in the measured pore pressure data have made them difficult to analyse and draw conclusions from. One source for this, could be that the piezometers were not allowed to properly stabilise enough, before the excavation at Brf. Sydney started. The action of driving the piezometers into the ground causes an increase in excess pore pressures, similar to piling but at a smaller scael. Usually this excess pore pressure stabilises after some time, and should be accounted for when planning the field-measurement program. In this case, the excavations started 3- 10 days after the piezometers were installed. This made it difficult to determine whether the observed pore pressure decrease were a result of the piezometers trying to reach the static level and/or was caused by the excavation.

With several construction projects taking place around Brf. Sydney at the time of writing, it is not unlikely that the surroundings could have affected the excess pore pressures in the studied area. As mentioned in chapter 3, Brf. Sydney is one among several constructions taking place in the area of Masthuggskajen. These neighbouring constructions, both finished and unfinished, will presumably have some kind of impact on the pore pressures in the ground beneath Brf. Sydney. Due to how the stresses in the soil caused by a load distribute over a larger width with increasing depth, the effects of surrounding constructions might have an impact on the pore pressures at larger depths. Displacements caused by piling in neighbouring constructions might also have an effect on the pore pressures beneath Brf. Sydney.

When comparing the measured pore pressure to the computed results in Figure 5.15, they showed mainly differences and some similarities. The monitored pore pressures below level -8 meter (10 m depth), are unaffected by the excavation of the center zone. The first excavation phase shows a decrease in pore pressure for both the measured and computed results, however, the decrease associated with the measured pore pressure could also be due to their stabilisation towards static level. The uncertainty of the decrease is based upon the fact that the excavation started promptly after the piezometers were installed and that they potentially did not stabilise, but also because the excavation of the center zone was more substantial and should show a greater response than the first excavation phase.
The measured pore pressure data were compared to the results of the calculations using Boussinesq's method. The comparisons showed that for Boussinesq's results, the unloading has a larger impact on the excess pore pressures closer to the surface, due to how the load diffuses with depth. This behaviour is not apparent in the results from the numerical model. However, due to modelling an idealised 1D unit cell. The unloading in the Boussinesq result are instantaneous, whereas the excavation in Plaxis goes on for 51 days. This means that the negative excess pore pressures generated by the unloading, dissipates as the excavation goes on. Furthermore, both the left and right hydraulic boundary is closed, meaning that the excess pore pressures are only allowed to drain in the vertical direction. This likely causes the generated negative excess pore pressures to redistribute throughout the depth, which results in negative excess pore pressures concentrating toward the halfway depth of modelled unit cell.

6.2 Piling

There are some factors regarding the piling that were not accounted for, which could effect the result in the numerical analysis. The actual pile driving process and rate is not considered, rather the pile instantaneously appears in the ground in the simulations. Allowing the cavity to expand over a short time might yield a slightly different result, it could possibly generate a lower immediate response as the pile is gradually expanding. Furthermore, this study disregards any vertical load being exerted on the pile and any resistance around the shaft of the pile, potentially affecting the displacements close to the pile and the heave. The resistance between the pile and soil could prevent some heave, as the piles in the ground acts as reinforcement of the soil (Tornborg, 2017). If this was modelled it could possibly lead to a decrease in vertical displacements.

The pre-augering of the first 15 m of the pile is represented by simply not expanding this part of the soil/pile in the numerical model. Neither is the soil removed or replaced with another material, (removing the soil without adding another material caused the soil to collapse and fail in the model). In reality, pre-augering would not totally diminish the displacement of the soil, as in practice it is difficult to remove the exact same amount of soil as the volume of the pile. The displacement would consequently lead to a change in pore pressure, however not as large as where it is not pre-augered. In Figure 5.3 it can be observed that the pore pressure is seemingly unaffected at depths of 10m and 15m, where it is pre-augered, whereas the nearby pile installation has an apparent effect on the depths of 20m and 40m. One thing to bear in mind is that the piezometers are placed 3-6 meters from the nearby piles, however, the majority of the piles at the site had no significant effect on the measured pore pressure. This indicates that the immediate change in pore pressure is quite isolated to the plastic zone around the pile. Since no mass is displaced at 5-, 10- and 15 meters depth, the magnitude of the negative excess pore pressures is lower at these depths.

The reason of the seemingly large excess pore pressures generated during piling when using Modified Cam Clay model, was hard to isolate. As previously stated, attempts were made to vary the compression index λ but this had no apparent effect. Chen and Abousleiman (2012) method appears to yield excess pore pressures closer to the Mohr-Coulomb and Randolph results, using a semi-analytical. It is speculated that these high pressures stem from the fact that the stress path of the soil close to the pile, reaches the yield surface in the MCC model and critical state. The soil by the pile also perhaps want to compress more than it's allowed to do. Finally, the relationship between K_{nc}^{0} and M in the Modified Cam Clay model in Plaxis (see Equation 2.34), might have lead to a incorrectly estimated shear strength. This might have yielded overestimated excess pore pressures, due to the proportionality between undrained shear strength and excess pore pressures observed in literature (Randolph and Wroth, 1979, Randolph et al., 1979, Randolph, 2003).

One interesting result of the parameter study is the effect soil stiffness has on EHP, when simulating both piling and excavating. That is, a higher soil stiffness is associated with less EHP, which is not observed when only simulating excavation. Considering how M_0 is related to G, and how G influences the generation and dissipation of excess pore pressures caused by piling, (see section 2.5 and 4.2.2.1) an increase in soil stiffness could correlate to less EHP in theory when piling.

6.3 Unloading

How the excess pore pressures dissipate throughout the depth during consolidation is comparable to Terzaghis theory. Since the model restricts flow in the horizontal boundaries, meaning that the only drainage paths are the top and bottom vertical boundary, thus, the model drains as Terzaghis solution with double-sided drainage.

This means that the pore pressures close to the halfway depth of the model will become larger than the pressures close to the boundaries.

The results from the unloading model (see Figure 5.9) yields a maximum normalised EHP equal to 0.78. The reason why this is not equal to 1 for the case of only unloading, is likely due to the unloading model simulating the Brf. Sydney construction sequence prior to varying t$_{exc.toslab}$. This includes the prolonged excavation procedure into the model (see Table 4.7), meaning that the excavation is allowed to consolidate (for 211 days), before it's fully completed. The effect of this prolonged excavation time becomes clear when comparing the results of the unloading model, to the results of the parametric study with varying permeability (see Figure 5.16), where an idealised excavation sequence of 1 day (see Table 4.9) is simulated. This yields a normalised EHP almost equal to one, due to the excavation not being allowed to consolidate before varying the time between excavation and slab installation.

The unloading model, as well as the models used in the parametric study, are all limited to one excavation depth of 4 m, and one uniform clay layer with a thickness of 100 m. Varying these parameters will impact the results, since they determine the length of the drainage path, and is included in the normalised time T_v. Varying these parameters as part of a parametric study on this topic, could help with understanding the how the excavation depth and drainage length impact the result.

6.4 Constitutive models

The constitutive models used in the numerical model does not account for creep behavior. Using models that account for creep such as Soft Soil Creep or Creep-SCLAY1S could have yielded a different result. However, these models require model parameters which adds complexity to the analysis. Deriving values for these parameters is not always an easy task and can be time-consuming, and could increase the risk of errors in the model, if not done properly..

There were uncertainties in deriving the stiffness parameter of the soil. Whether to use the empirical formula $M_0 = 250c_u$ or $M_0 = 500c_u$ was discussed, and the choice of $M_0 = 500c_u$ was primarily based on the fact that the OCR at Brf. Sydney is closer to 1, whereas $M_0 = 250c_u$ is applicable for soils with an OCR of 3 (see section 2.2.1). The stiffness in the constitutive models were plotted against depth, where it was compared to the multiplied compression modulus derived from the CRS tests. This further showed that assuming $M_0 = 500c_u$ was representative for the soil at Brf. Sydney. But as the in situstiffness is difficult to derive, the stiffness was varied in the parametric study to see the impact on the EHP. This was done to generalise the study, for it to be applicable to more cases than for Brf. Sydney.

The groundwater table was set to excavation bottom for the final excavation step. The groundwater table was therefore assumed to be at excavation bottom for the soil cluster between level -2 m and -17 meter. In the soil cluster below this level, the original groundwater table at +0.5 m was used. For further studies the groundwater table could have be set to global level (+0.5) after the excavation step to see how this effects the effective heave pressure.

7

Conclusions and recommendations

This thesis aimed to study the combined impact of pile driving and excavation have on the development and evolution of excess pore pressure, heave, and heave pressure. For the aim to be achieved pore pressure data from a specific construction project was collected, the monitoring data was compared to analytical, and numerical calculations. Furthermore, a parametric study was conducted to generalise the results and study the impact of varying chosen soil parameters. The main conclusions from this study are:

- The results indicate that positive excess pore pressures caused by piling have the potential to counteract the negative excess pore pressures generated by excavation, leading to a reduction of heave pressure on the slab.

- Furthermore, results also show that piling before or after excavating generates different amounts of vertical displacements. Piling before excavating seems to reduce vertical displacement. The vertical displacements when excavating after pile driving would be further reduced if the nailing effect of the pile elements were to be considered.

- Both excess pore pressure and heave caused by unloading and piling are complex problems to compute in themselves. Studying the combination of these is therefore undoubtedly complex as well. Idealisation such as a unit cell geometry was adopted with respect to the scope of this work.

- A majority of the measured pore pressure data from Brf. Sydney was deemed partly insufficient as unexplained irregularities in the data were observed for both the piezometers at elevations -18 and -38 meters. The cause of these irregularities has not been determined.

- The Mohr-Coulomb model proved to be efficient in modeling the pore pressure response during piling. In this analysis, the Modified Cam Clay model did not yield a similar response when compared to analytical solutions and the Mohr-Coulomb model, with regard to excesss pore pressures.

Further studies could build upon the analysis conducted in this thesis, and include more factors to increase the complexity sequentially. Listed below, are recommendations for further studies regarding the combined impact that piling and excavation have in terms of pore pressure, heave, and heave pressure.

- Modelling the actual pile element in addition to expanding a cavity, could be useful to further study the effects piling might have on the heave pressure and excess pore pressure. This would mainly incorporate the effects of the interface between the pile and the soil, such as the reinforcing (soil nailing) effect after pile installation. Furthermore, whether there are any significant effects on excess pore pressures and heave, with a load being exerted on the pile could also be studied. This would, in combination with a soil model that accounts for creep (see final recommendation), enable to study the evolution of tension and/or compression loads in piles over time.

- Studying the combined effects of a group of piles with regard to excess pore pressures and heave might prove useful in assessing the heave pressure in practical construction cases. Determining if the magnitude of the excess pore pressures scales with the number of piles, and how the effect of the installation pattern affects excess pore pressure and heave, could help in developing a reliable analytical method to estimate the heave pressure on a slab. Randolph's theory on excess pore pressures due to pile driving could perhaps be incorporated into this type of study, to be modified and extrapolated to study the effects of a group of piles.

- Finally, conducting a numerical analysis similar to this one, but with a more sophisticated constitutive model, could refine the findings of this study. This would, for instance, incorporate creep effects into the model. The computed magnitude of such effects could also help with determining whether they need to be accounted for when studying this behavior in practice.

Bibliography

Alén, C. (1998). *On Probability in Geotechnics. Random Calculation Models Exemplified on Slope Stability Analysis and Ground-Superstructure Interaction* (tech. rep.). https://research.chalmers.se/en/publication/927

Baligh, M. M. (1986). Undrained deep penetration, I: shear stresses. *Géotechnique*, *36*(4), 471–485. https://doi.org/10.1680/GEOT.1986.36.4.471

Bentley. (2023a). *PLAXIS; Material models manual 2D* (tech. rep.).

Bentley. (2023b). *PLAXIS; Reference Manual 2D* (tech. rep.).

Brinkgreve, R. B. J. (2005). Selection of Soil Models and Parameters for Geotechnical Engineering Application. *Soil Constitutive Models*, 69–98. https://doi.org/10.1061/40771(169)4

Chen, S. L., & Abousleiman, Y. N. (2012). Exact undrained elasto-plastic solution for cylindrical cavity expansion in modified Cam Clay soil. *Géotechnique*, *62*(5), 447–456.

ELU Konsult AB. (2021, June). *PM Geoteknik: RBA Masthuggskajen Hus E3, Brf Sydney* (tech. rep.).

Geotech AB. (2024). PVT Direct push piezometer.

Göteborgs Stad. (2018). *Detaljplan för Järnvågsgatan m.fl. inom stadsdelen Majorna-Linné i Göteborg* (tech. rep.).

Göteborgs Stad. (2022). Översiktsplan för Göteborg. https://goteborg.se/wps/portal?uri=gbglnk:gbg.page.bb7386fd-1152-47cb-9da4-d06bd7780a77&projektid=BN0199/17

Hansbo, S. (1990). *Jordmekanik 1 Spänningar av yttre last, sättningar, jordtryck.* Chalmers University of Technology.

Hintze, S., Liedberg, S., Massarsch, R., Hansson, M., Elvhammar, H., Lundahl, B., & Rehnman, S.-E. (1997). *Rapport 95, omgivningspåverkan vid pål- och spontslagning* (tech. rep.). Pålkommisionen. Linköping.

Isaksson, J. (2022). *A numerical study on mass displacements from piling in natural clay* (tech. rep.). Chalmers University of Technology. Gothenburg.

Jansson, C. (2024). Communication with supervisor, Brf. Sydney.

Karstunen, M., & Amavasai, A. (2017). *BEST SOIL: Soft soil modelling and parameter determination* (tech. rep.).

Kempfert, H.-G., & Gebreselassie, B. (2010, October). *Excavations and Foundations in Soft Soils* (1st ed.). Springer. https://doi.org/10.1007/3-540-32895-5

Knappett, J., & Craig, R. F. (2012). *Craig's soil mechanics.*

Larsson, R. (1986). *Report No 29, Consolidation of soft soils* (tech. rep.). Swedish Geotechnical Institute. Linköping.

Larsson, R. (2008). *Jords egenskaper* (tech. rep.). Swedish Geotechnical Institute. Linköping, Statens geotekniska institut. https://urn.kb.se/resolve?urn=urn:nbn:se:swedgeo:diva-142

Lo, K. Y., & Stermac, A. G. (1965). Induced Pore Pressures During Pile-Driving Operations. *Proceedings 6th International Conference on Soil Mechanics and Foundation Engineering, vol 2,* 285–289.

Lo, K. Y. (1968). Discussion of: Effects of pile driving on soil properties. *Journal of the Soil Mechanics and Foundation Division*, *94*(2), 606–608.

Masthuggskajen. (n.d.). Så utvecklas Masthuggskajen. https://masthuggskajen.se/projektet/

Muir Wood, D. (2004). *Geotechnical Modelling* (1st ed.). Taylor; Francis.

Persson, J. (2004). *The Unloading Modulus of Soft Clay: A Field and Laboratory study* [Doctoral dissertation, Chalmers University of Technology].

Pestana, J. M., Hunt, C. E., & Bray, J. D. (2002). Soil Deformation and Excess Pore Pressure Field around a Closed-Ended Pile. *Journal of Geotechnical and Geoenvironmental Engineering*, *128*(1), 1–12. https://doi.org/10.1061/(ASCE)1090-0241(2002)128:1(1)

Randolph, M. F. (2003). Science and empiricism in pile foundation design. *Géotechnique*, *53*(10), 847–875. https://doi.org/10.1680/GEOT.2003.53.10.847

Randolph, M. F., Carter, J. P., & Wroth, C. P. (1979). Driven Piles in clay—The Effects of Installation and Subsequent Consolidation. *Geotechnique*, *29*(4), 361–393. https://doi.org/10.1680/GEOT.1979.29.4.361

Randolph, M. F., & Wroth, C. P. (1979). An analytical solution for the consolidation around a driven pile. *International Journal for Numerical and Analytical Methods in Geomechanics*, *3*(3), 217–229. https://doi.org/10.1002/NAG.1610030302

Roscoe, K. H., & Burland, J. B. (1968a). On the Generalized Stress-Strain Behaviour of Wet Clay.

Roscoe, K. H., & Burland, J. B. (1968b, March). On the Generalized Stress-Strain Behavior of Wet Clays. In J. Heyman (Ed.), *Engineering plasticity* (pp. 535–609).

Sällfors, G. (2013). *Geoteknik*. Chalmers University of Technology.

Schager, E. (2017). *Spår av de gamla hamnarna i Masthuggskajen* (tech. rep.). Arkeologerna.

Schofield, A. N., & Wroth, C. P. (1968). *Critical State Soil Mechanics*. McGraw-Hill.

Skanska. (2022a). Skanska bygger flerfamiljshus åt Riksbyggen i Göteborg för cirka 330 miljoner kronor. https://www.skanska.se/om-skanska/press/pressmeddelanden/269530/Skanska-bygger-flerfamiljshus-at-Riksbyggen-i-Goteborg-for-cirka-330-miljoner-kronor

Skanska. (2022b). *Underlag för utformning av temporär spont, byggnadens pålgrundläggning samt kontakttrycket mot dess bottenplatta* (tech. rep.).

Skanska Teknik. (2023, May). Construction Document for Brf. Sydney. Job nr: 210577.

Skempton, A. (1954). The Pore-Pressure Coefficients A and B. *Géotechnique*, *4*(4), 143–147. https://doi.org/10.1680/GEOT.1954.4.4.143

Sun, D., Yao, Y.-P., & Matsuoka, H. (2006). Modification of critical state models by Mohr–Coulomb criterion.

Terzaghi, K. (1943). *Theoretical Soil Mechanics*. John Wiley & Sons.

Tornborg, J. (2017). *Svälltryck på grund av avlastning i lös lera; Studie av hävningsförlopp och potentiella följdeffekter* (tech. rep.).

Tornborg, J., Karlsson, M., Dijkstra, J., & Karstunen, M. (2024). On the development of effective heave pressure in deep excavations. (Manuscript under review at journal paper).

Tornborg, J., Karlsson, M., Kullingsjö, A., & Karstunen, M. (2021). Modelling the construction and long-term response of Göta Tunnel. *Computers and Geotechnics*, *134*. https://doi.org/https://doi.org/10.1016/j.compgeo.2021.104027.

Verruijt, A. (2017). *An introduction to soil mechanics* (1st ed.). Springer Cham. https://doi.org/https://doi.org/10.1007/978-3-319-61185-3

Verruijt, A., & Merwehoofd, A. V. (1994). *Offshore Soil Mechanics* (tech. rep.). http://geo.verruijt.net

Vesić, A. S. (1972). Expansion of Cavities in Infinite Soil Mass. *Journal of the Soil Mechanics and Foundations Division*, *98*(3).